CMD® 第47回　先端研究事例講義
(CMD® Case Studies)

石橋 章司

筑波大学 計算科学研究センター

産業技術総合研究所 エレクトロニクス基盤技術研究部門

Shoji ISHIBASHI

Center for Computational Sciences (CCS), University of Tsukuba

Core Electronics Technology Research Institute (CETRI),
National Institute of Advanced Industrial Science and Technology (AIST)

Outline

Overview of the computational code QMAS

Applications of QMAS's distinctive calculation functions

- Positron annihilation
- Static electric field
- Stress density

Release of QMAS Fortran90 beta version

Outline

Overview of the computational code QMAS

Applications of QMAS's distinctive calculation functions

- Positron annihilation
- Static electric field
- Stress density

Release of QMAS Fortran90 beta version

Projector Augmented-Wave (PAW) method

Blöchl, Phys. Rev. B **50**, 17953 (1994).

$$|\Psi_n\rangle = |\tilde{\Psi}_n\rangle + \sum_i \left(|\phi_i\rangle - |\tilde{\phi}_i\rangle\right)\langle \tilde{p}_i | \tilde{\Psi}_n\rangle$$

$$\langle \tilde{p}_i | \tilde{\phi}_j \rangle = \delta_{ij}$$

$$E = \tilde{E} + E^1 - \tilde{E}^1$$

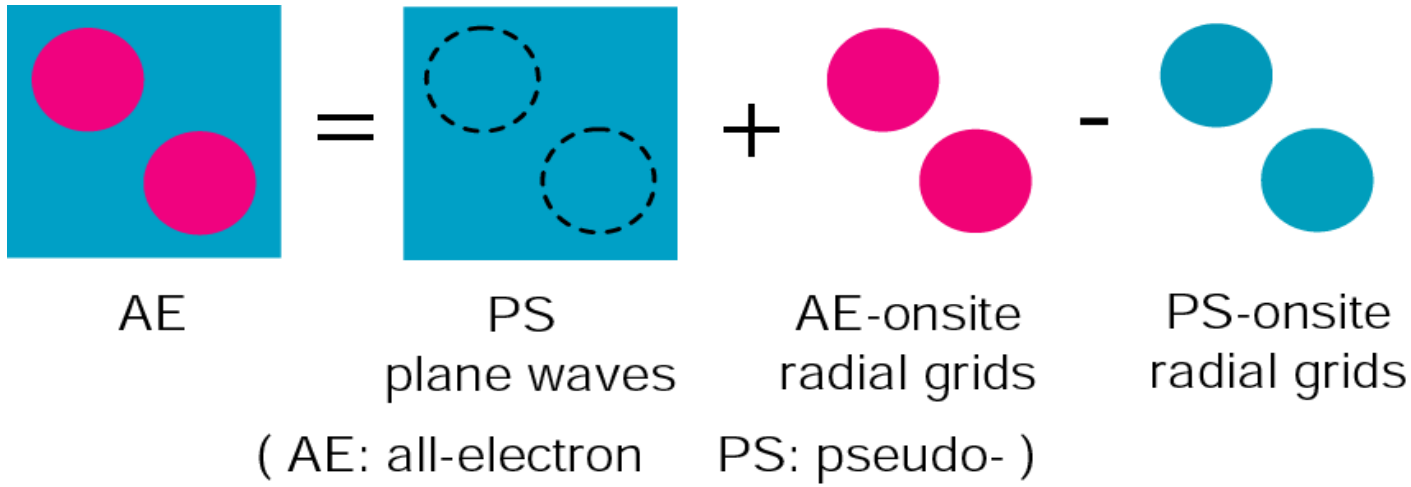

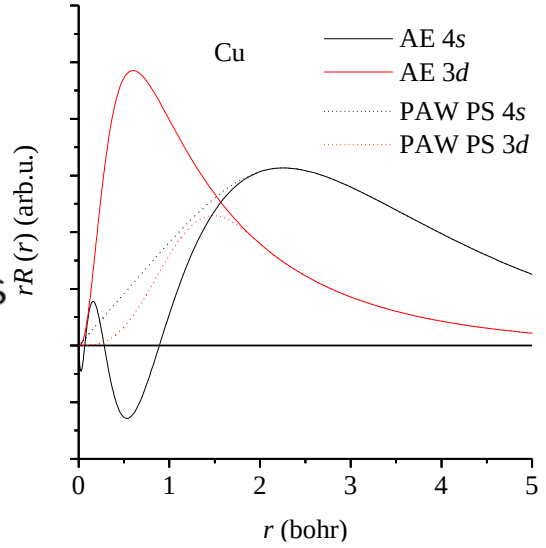

- The number of plane waves can be drastically reduced.
- All-electron wavefunctions are available and accuracy in estimating physical properties is improved.

Prototype of QMAS

S. Ishibashi, Material Science Forum **445-446**, 401 (2004).

The purpose was to reconstruct accurate wave functions from the results of NCPP calculations based on the method for USPP proposed by Hetényi et al. [J. Chem. Phys. **115**, 5791 (2001)], and to obtain the momentum distribution of electron-positron annihilation gamma rays. Since the calculation results of the PAW method were needed as a reference, a calculation program for the PAW method was completed (the prototype of QMAS). I never used this reconstruction technique again.

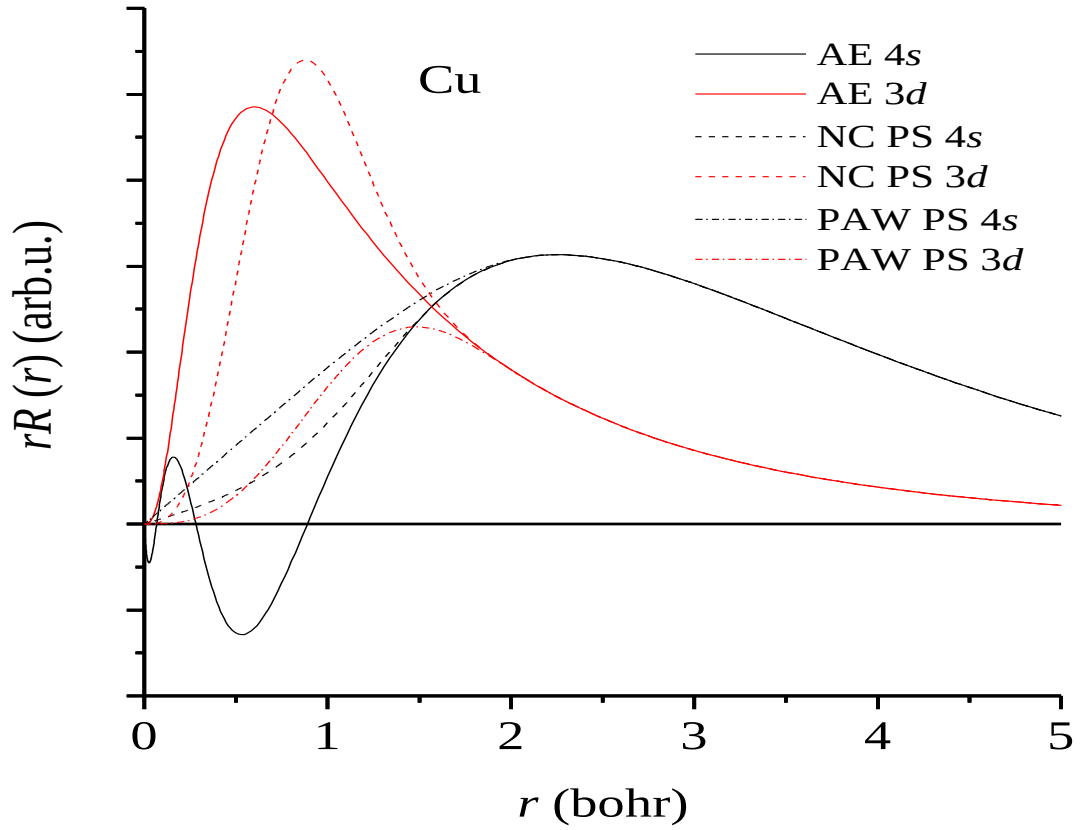

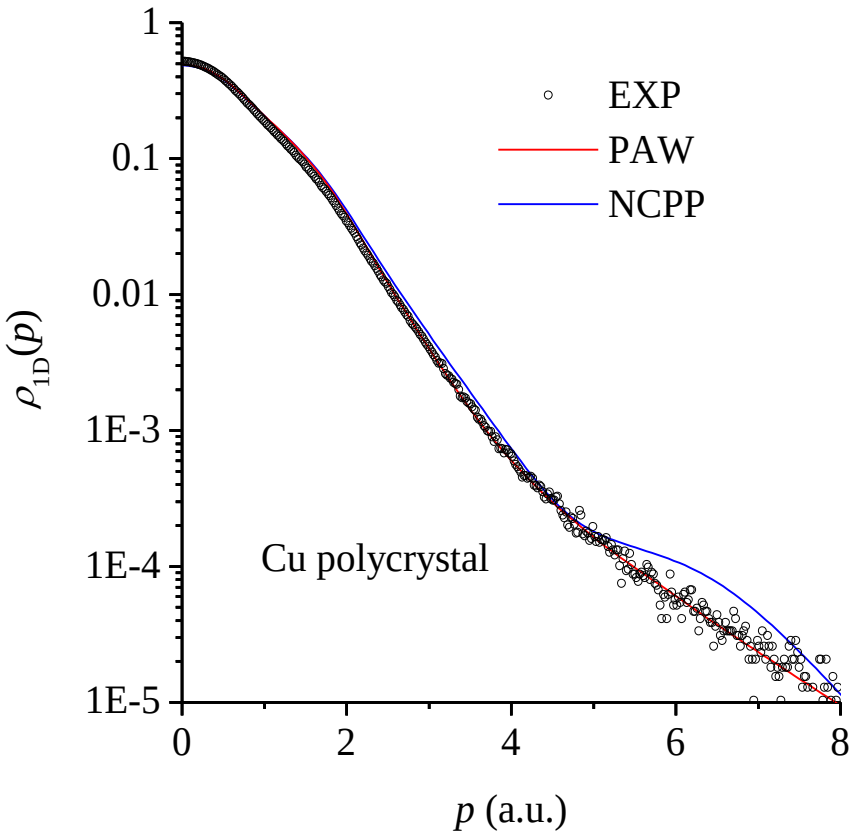

QMAS

(Quantum MAterials Simulator) http://qmas.jp

QMAS is a first-principles computational tool, which is based on the density functional theory, to study various structural and electronic properties of materials. The projector augmented-wave (PAW) method with plane wave basis set is adopted.

- Efficient parallel computation with hybrid MPI/OpenMP
- Force and stress calculations for structural optimization
- local analyses of electronic structures (through local/partial DOS, Mulliken/Bader charges)
- Local Density Approximation (LDA) and Generalized Gradient Approximation (GGA)
- Use of on-site Coulomb interaction *U* (LDA/GGA+*U*) for strongly-correlated electron system
- van der Waals DFT (vdW-DF-cx, rVV10)
- **Calculation of positron states and annihilation parameters**
- Calculation of electronic polarization through Berry's phase
- **Electronic-structure calculation under static electric field**
- **Calculation of** energy density and **stress density**
- Electrochemical study with the effective screening medium (ESM) method
- Calculation of atomic-scale dielectric permittivity
- Spin-orbit interaction and non-collinear magnetism with two-component spinor formalism

Published papers using QMAS

https://qmas.jp/pub/index.html

Publications

(2025)

1. Field-Effect Crystal Engineering in Proton-π-Electron Correlated Systems,
   S. Horiuchi, H. Minemawari, J. Tsutsumi and S. Ishibashi,
   Crystals **15**, 736 (2025).

2. Anion adsorption-induced charge separation at the alumina/aluminum interface,
   S. Hagiwata, T. Murata and M. Otani,
   Corrosion Sci. **256**, 113150 (2025).

3. Roles of Al-vacancy complexes on the luminescence spectra of low dislocation density Si-doped AlN grown by halide vapor phase epitaxy,
   S.F. Chichibu, K. Kikuchi, B. Moody, S. Mita, R. Collazo, Z. Sitar, Y. Kumagai, S. Ishibashi, A. Uedono and K. Shima,
   Appl. Phys. Lett. **126**, 111905 (2025).

4. Unveiling High Electro-Optic Performance in a Proton-π-Electron-Coupled Ferroelectric Crystal,
   K. Sunami, S. Horiuchi, S. Ishibashi and J. Tsutsumi,
   Adv. Electron. Mater. **11**, 2400346 (2025).

(2024)

5. Bias-dependent surface stress by density functional theory combined with the effective screening medium method,
   S. Hagiwara, S. Ishibashi and M. Otani,
   Phys. Rev. B **110**, 155409 (2024).

6. Vacancy-Type Defects and Oxygen Incorporation in NiAl for Advanced Interconnects Probed by Monoenergetic Positron Beams and Atom Probe Tomography,
   A. Uedono, C. Fleischmann, J.-P. Soulié, M. Ayyad, J.E. Scheerder, C. Adelmann, J. Uzuhashi, T. Ohkubo, K. Michishio, N. Oshima and S. Ishibashi,
   ACS Appl. Electron. Mater. **6**, 5894 (2024).

7. Impacts of vacancy complexes on the room-temperature photoluminescence lifetimes of state-of-the-art GaN substrates, epitaxial layers, and Mg-implanted layers,
   S.F. Chichibu, K. Shima, A. Uedono, S. Ishibashi, H. Iguchi, T. Narita, K. Kataoka, R. Tanaka, S. Takashima, K. Ueno, M. Edo, H. Watanabe, A. Tanaka, Y. Honda, J. Suda, H. Amano, T. Kachi, T. Nabatame, Y. Irokawa and Y. Koide,
   J. Appl. Phys. **135**, 185701 (2024).

8. Vacancy-Type Defects and Their Trapping/Detrapping of Charge Carriers in Ion-Implanted GaN Studied by Positron Annihilation,
   A. Uedono, R. Tanaka, S. Takashima, K. Ueno, M. Edo, K. Shima, S.F. Chichibu, J. Uzuhashi, T. Ohkubo, S. Ishibashi, K. Sierakowski and M. Bockowski,
   Phys. Stat. Sol. (b) **261**, 2400060 (2024).

155. First-principles analysis of the optical properties of structural disorder in SiO_2 glass,
    T. Tamura, S. Ishibashi, S. Tanaka, M. Kohyama, and M. -H. Lee,
    Phys. Rev. B **77**, 085207 (2008).

156. Electronic structures of single component molecular metals based on ab initio calculation,
    S. Ishibashi, K. Terakura and A. Kobayashi,
    J. Phys. Soc. Jpn. **77**, 024702 (2008).

157. First-principles calculations of Pd/Au(100) interfaces with adsorbates,
    S. Tanaka, N. Taguchi, T. Akita, F. Hori and M. Kohyama,
    Solid State Phenom. **139**, 47 (2008).

158. First-principles calculations of the atomic and electronic structures in Au-Pd slab interfaces,
    N. Taguchi, S. Tanaka, T. Akita, M. Kohyama and F. Hori,
    Solid State Phenom. **139**, 29 (2008).

(2007)

159. Annealing properties of vacancy-type defects in ion-implanted GaN studied by monoenergetic positron beams,
    A. Uedono, K. Ito, H.nakamori. K. Mori, Y. Nakano, T. Kachi, S. Ishibashi, T. Ohdaira and R. Suzuki,
    J. Appl. Phys. **102**, 084505 (2007).

160. Vacancy-fluorine complexes and their impact on the properties of metal-oxide transistors with high-k gate dielectrics studied using monoenergetic positron beams,
    A. Uedono, S. Inumiya, T. Matsuki, T. Aoyama, Y. Nara, S. Ishibashi, T. Ohdaira, R. Suzuki, S. Miyazaki and K. Yamada,
    J. Appl. Phys. **102**, 054511 (2007).

161. Ab initio calculations of electric-field-induced stress profiles for diamond/c-BN(110) superlattices,
    S. Ishibashi, T. Tamura, S. Tanaka, M. Kohyama, and K. Terakura,
    Phys. Rev. B **76**, 153310 (2007).

162. Static dielectric response and Born effective charge of BN nanotubes from ab initio finite electric field calculations,
    G. Y. Guo, S. Ishibashi, T. Tamura and K. Terakura,
    Phys. Rev. B **75**, 245403 (2007).

163. Schottky-barrier heights of metal/alpha-SiC{0001} interfaces by first-principles calculations,
    S. Tanaka, T. Tamura, K. Okazaki, S. Ishibashi and M. Kohyama,
    phys. stat. soli. (c) **4**, 2972 (2007).

(2006)

164. Vacancy-impurity complexes in polycrystalline Si used as gate electrodes of HfSiON-based metal-oxide-semiconductors probed using monoenergetic positron beams,
    A. Uedono, K. Ikeuchi, T. Otsuka, K. Yamabe, K. Eguchi, M. Takayanagi, S. Ishibashi, T. Ohdaira, M. Muramatsu and R. Suzuki,
    J. Appl. Phys. **100**, 034509 (2006).

165. First-principles calculations of Schottky barrier heights of monolayer metal/6H-SiC{0001} interfaces,
    S. Tanaka, T. Tamura, K. Okazaki, S. Ishibashi and M. Kohyama,
    Mater. Trans. **47**, 2690 (2006).

166. Ab initio electronic-structure calculations for alpha-$(BEDT\text{-}TTF)_2I_3$,
    S. Ishibashi, T. Tamura, M. Kohyama and K. Terakura,
    J. Phys. Soc. Jpn. **75**, 015005 (2006).

Outline

Overview of the computational code QMAS

Applications of QMAS's distinctive calculation functions

- Positron annihilation
- Static electric field
- Stress density

Release of QMAS Fortran90 beta version

Positron in solids

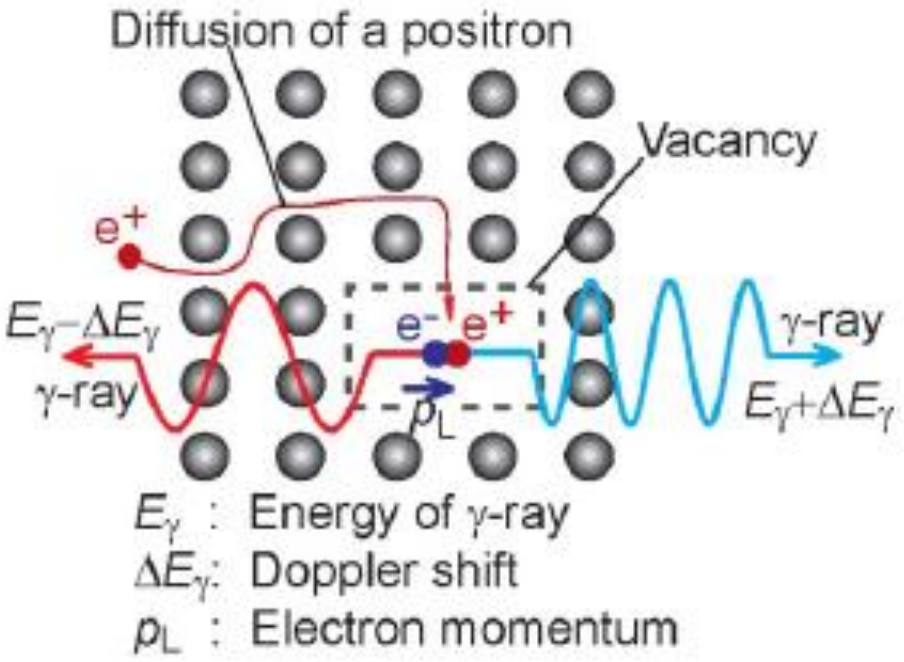

A positron annihilates with an electron in solid emitting gamma rays.

Positron annihilation method

- Momentum distribution
- Positron Lifetime

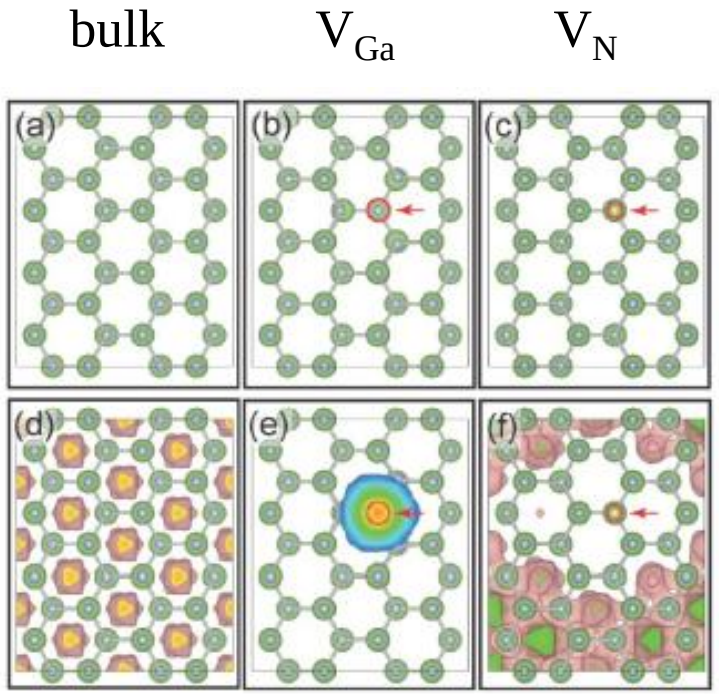

Positron are selectively trapped at the Ga vacancy in GaN.

A. Uedono, S. Ishibashi, S.F. Chichibu and K. Akimoto, Gallium Nitride Materials and Devices VI, Proc. of SPIE Vol. 7939, 79390I (2011).

Two modes for momentum distribution measurements

Angular correlation

- high resolution, low efficiency

accurate measurements of **2D** momentum distributions in a lower momentum region

=> *e.g.*, Fermiology

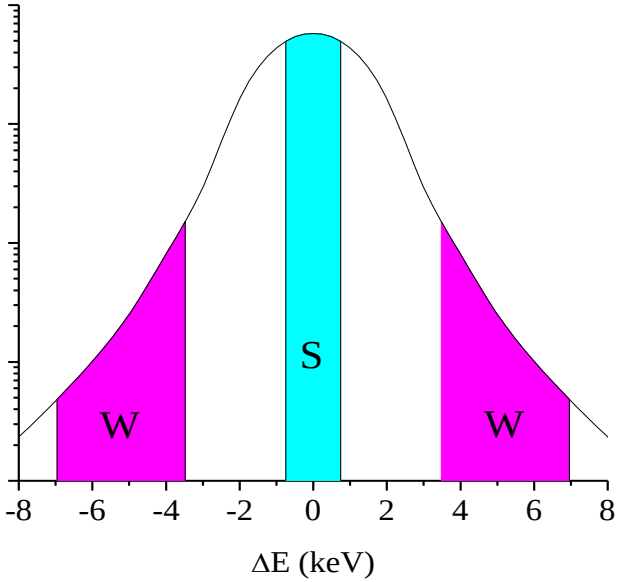

Doppler broadening

- low resolution, high efficiency (high statistical accuracy)

rapid measurements of overall shapes of **1D** momentum distributions

=> defect spectroscopy through **S** and **W** parameters

distribution measurements in a higher momentum region

=> identification of atomic species surrounding defects through core electron momentum distribution measurements

Momentum distribution of annihilation radiations

Doppler broadening spectrum corresponds to 1D projection of the momentum distribution of annihilation radiations:

$$\rho(\mathbf{p}) \propto \sum_j \left| \int \psi_+(\mathbf{r}) \psi_{-j}(\mathbf{r}) \sqrt{\gamma(n_-(\mathbf{r}))} \exp(-i\mathbf{p}\cdot\mathbf{r}) d\mathbf{r} \right|^2, \qquad J(p_z) = \iint \rho(\mathbf{p}) dp_x dp_y$$

ρ : momentum distribution, ψ_+ : positron wavefunction,

ψ_{-j} : electron wavefunction of band j, γ : enhancement factor.

The above expression contains a Fourier transformation and spatial variations of overlaps between electron and positron wavefunctions are reflected.

=> The electronic wavefunctions should be accurately represented even in the vicinity of ion cores to describe the spectrum in a higher-momentum region correctly.

On the other hand, defect systems are often subjected to study and they inevitably contains many atoms in the unit cell considered in the calculation.

=> Highly efficient tool is demanded to determine atomic arrangements and obtain electronic wavefunctions.

The PAW method satisfies both the requirements.

Comparison of Doppler spectra between NCPP and PAW

S. Ishibashi, Material Science Forum 445-446, 401 (2004).

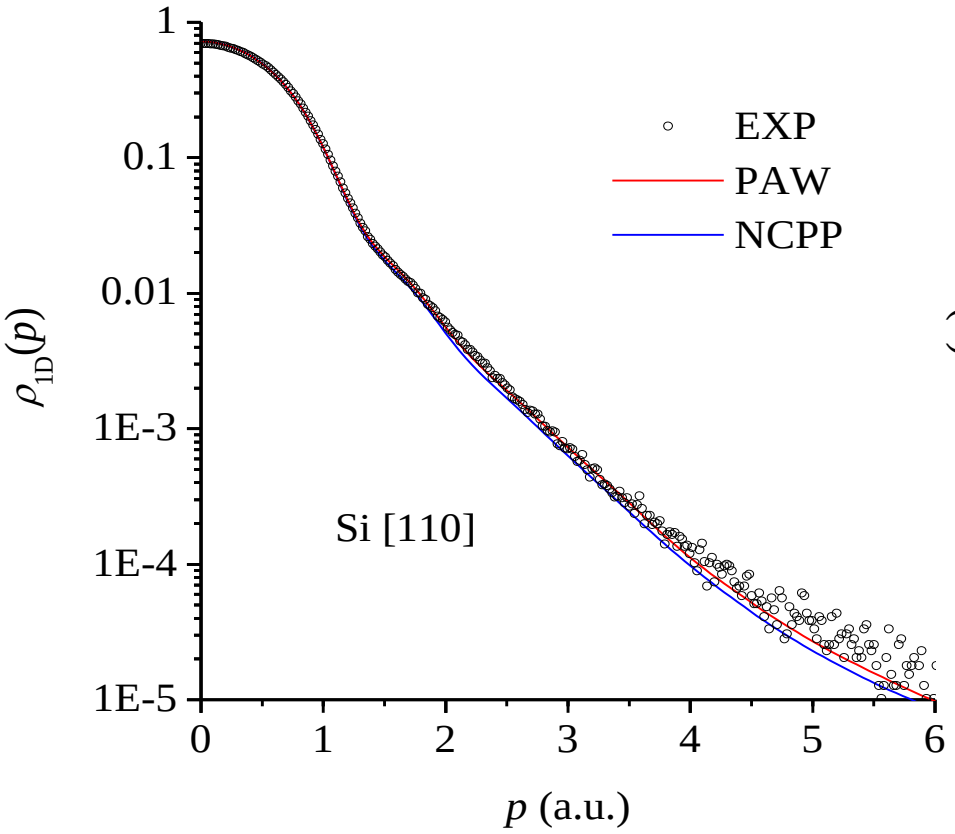

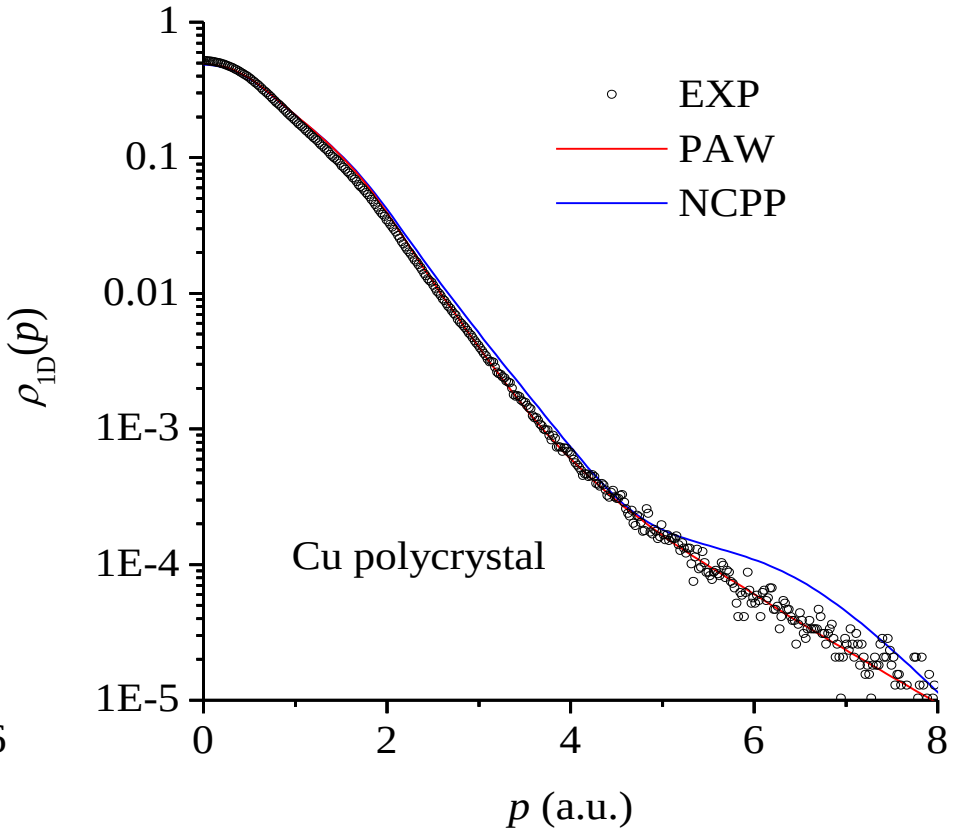

S,W parameters

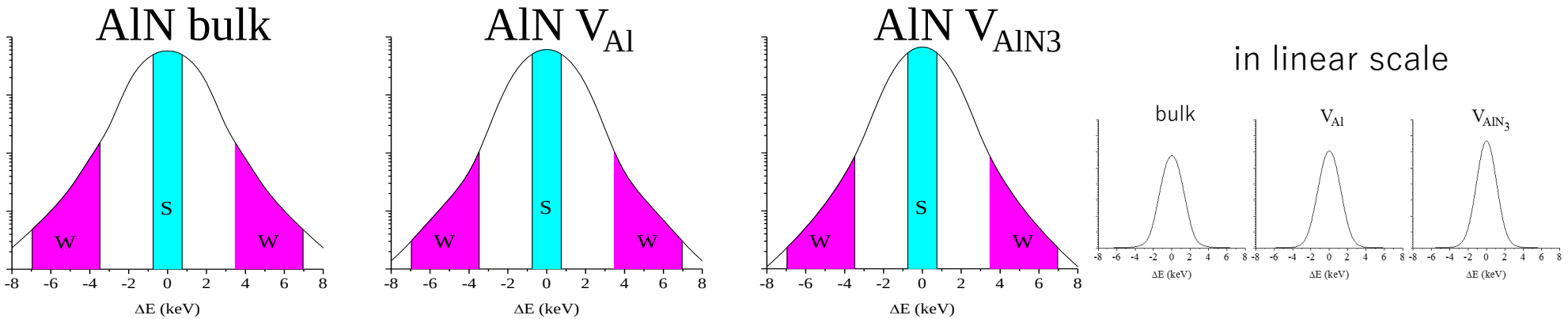

Increase of open volume＝＞narrowing of spectrum＝＞S up, W down

S-W plot

Describing parameters for the bulk as（S_b,W_b）and for a defect as（S_d,W_d）, observable（S_{obs},W_{obs}）is expressed as $S_{obs}=S_bF_b+S_dF_d$, $W_{obs}=W_bF_b+W_dF_d$ （$F_b+F_d=1$）

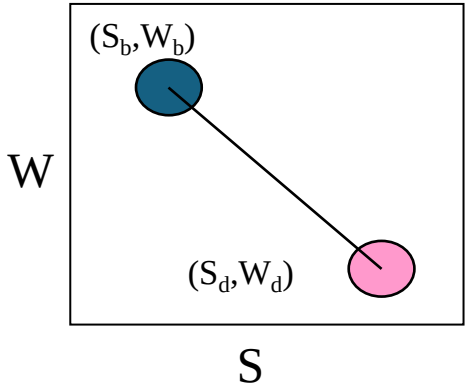

If positrons are trapped at one kind of defects（S_d,W_d）, observed (S,W) should be on the line.

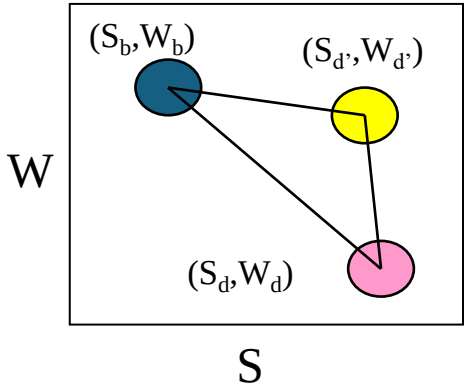

If positrons are trapped at two kinds of defects（S_d,W_d）, observed (S,W) should be inside the triangle.

Vacancy-type defects in AlN and GaN

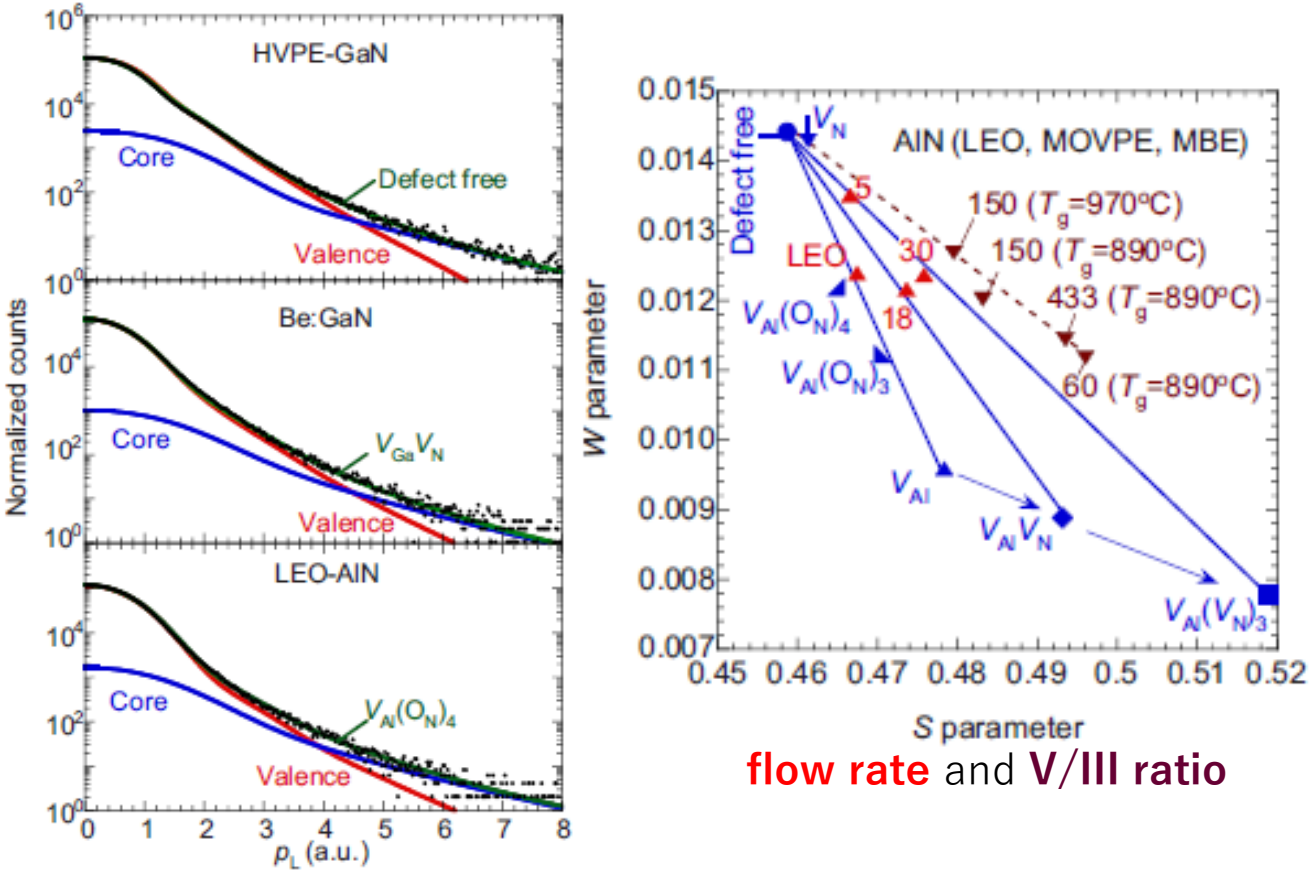

Vacancy type defects in AlN specimens prepared by metal-organic vapor phase epitaxy (MOVPE), molecular beam epitaxy (MBE) and lateral epitaxial overgrowth (LEO) are investigated. For MOVPE and MBE, the major defect species can be identified as vacancy cluster such as $V_{Al}(V_N)_n$ (n=1-3), while, for LEO, vacancy-oxygen complexes such as $V_{Al}(O_N)_n$ (n=3,4) seem to have significant contributions.

A. Uedono, S. Ishibashi, S. Keller, C. Moe, P. Cantu, T.M. Katona, D.S. Kamber, Y. Wu, E. Letts, S.A. Newman, S. Nakamura, J.S. Speck, U.K. Mishra, S.P. DenBaars, T. Onuma and S.F. Chichibu, J. Appl. Phys. **105**, 054501 (2009).

Outline

Overview of the computational code QMAS

Applications of QMAS's distinctive calculation functions

- Positron annihilation
- Static electric field
- Stress density

Release of QMAS Fortran90 beta version

References

Static electric field
Souza *et al.*: Phys. Rev. Lett. 89 (2002) 117602.; Phys. Rev. B 69 (2004) 085106.

Stress density
Fillippetti and Fiorentini, Phys. Rev. B **61** (2000) 8433.

1D (hermaphrodite) wannier function
Marzari and Vanderbilt, Phys. Rev. B **56** (1997) 12847.

Atomic-scale dielectric permittivity profile
Giustino and Pasquarello, Phys. Rev. B 71 (2005) 144104.

Calculation method for electronic states under electrostatic fields

I. Souza *et al.*: Phys. Rev. Lett. 89 (2002) 117602.; Phys. Rev. B 69 (2004) 085106.

The total energy E^F when an electrostatic field **E** is applied is represented as

$$E^{\mathrm{F}} = E^0 - \Omega \mathbf{P} \cdot \mathbf{E}$$

where E^0 is the energy at zero filed, Ω is the unit-cell volume, and **P** is the induced polarization. In such a case, the following term is added to Kohn-Sham Hamiltonian:

$$\frac{\delta\left(-\Omega \mathbf{P} \cdot \mathbf{E}\right)}{\delta\left\langle u_{n\mathbf{k}}\right|} = \frac{ife}{4\pi} \sum_{i=1}^{3} \frac{\mathbf{E} \cdot \mathbf{a}_i}{N_{\perp}^{(i)}} \sum_{m=1}^{M} \left[\left| u_{m,\mathbf{k}_{+}^{(i)}} \right\rangle \mathbf{S}_{mn}^{-1}\left(\mathbf{k}, \mathbf{k}_{+}^{(i)}\right) - \left| u_{m,\mathbf{k}_{-}^{(i)}} \right\rangle \mathbf{S}_{mn}^{-1}\left(\mathbf{k}, \mathbf{k}_{-}^{(i)}\right) \right]$$

where $u_{n\mathbf{k}}$, f , and $\mathbf{a}_{\mathrm{i}}$ are Bloch functions, occupation numbers, and lattice vectors, respectively.

$$N_{\perp}^{(1)} = N_2 \times N_3$$

$N_1 \times N_2 \times N_3$ is the number of **k** points in the Brillouin zone.

Examples of using electrostatic field calculations

Souza *et al.*: Phys. Rev. Lett. 89 (2002) 117602.; Phys. Rev. B 69 (2004) 085106.

Dielectric constant

The dielectric constant $\varepsilon_{\alpha\beta}$ is represented as

$$\varepsilon_{\alpha\beta} = \delta_{\alpha\beta} + \frac{1}{\varepsilon_0}\frac{\mathrm{d}\,\mathbf{P}_\alpha}{\mathrm{d}\,\mathbf{E}_\beta}$$

where ε_0 is the vacuum permittivity. If we calculate the above value with atomic positions fixed, the electronic dielectric constant ε_∞ can be obtained. If relaxed, the static dielectric constant ε_s is obtained.

Born effective charge

$$eZ^*_{j\alpha\beta} = \frac{\mathrm{d}\,\mathbf{F}_{j\beta}}{\mathrm{d}\,\mathbf{E}_\alpha}$$

Piezoelectric constants should be obtained from $c_{\alpha\beta\gamma} = \dfrac{\mathrm{d}\,\boldsymbol{\sigma}_{\beta\gamma}}{\mathrm{d}\,\mathbf{E}_\alpha}$

Dielectric constant

	ε_s (cell fixed)	ε_s (cell relaxed)	ε_∞	Z^*
SiC	**9.79**	**9.93**	**6.50**	**2.70**
	9.73	9.73	6.52	2.70
BN	**6.68**	**7.02**	**4.42**	**1.93**
	7.1	7.1	4.5	1.98
AlP	**10.18**	**9.88**	**7.57**	**2.24**
	9.8	9.8	7.5	2.28
Si	**12.39**	**12.39**	**12.39**	**0.00**
	12.0	12.0	12.0	0.00
C	**5.75**	**5.75**	**5.75**	**0.00**
	5.66	5.66	5.66	0.00

upper: calculations
lower: experimental values

Unlike using the KK transformation of the dielectric function, there is no overestimation of the dielectric constant due to an underestimation of the band gap.

Stress profiles in Diamond/BN superlattice

Diamond/BN 7+7 superlattice

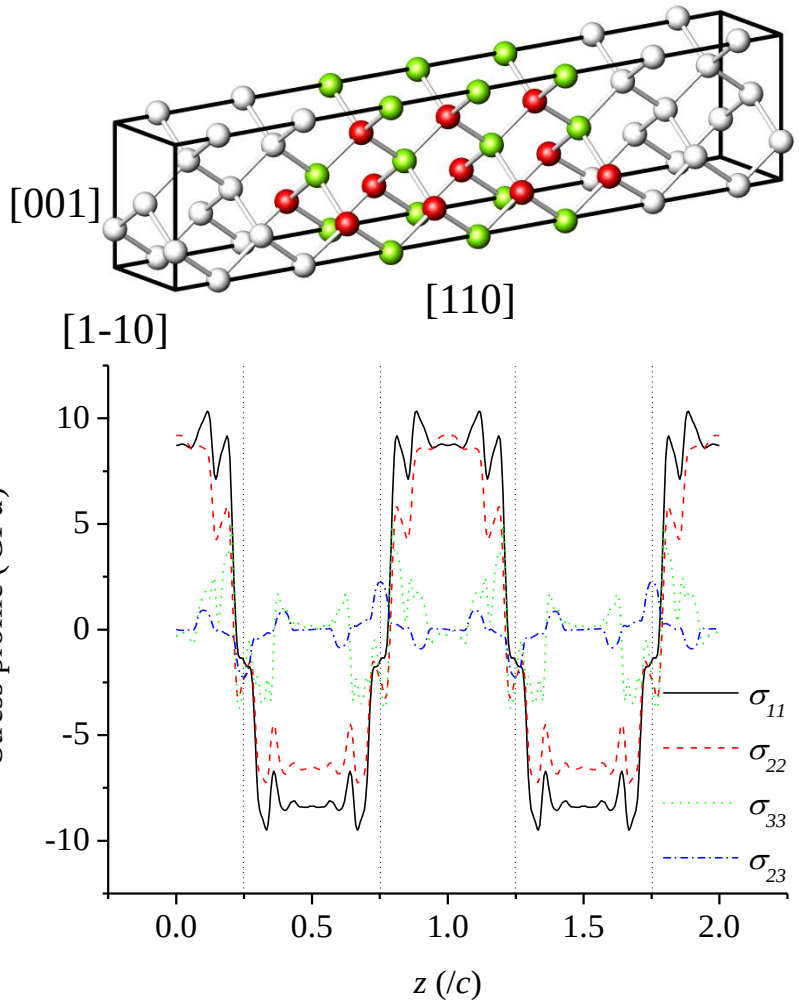

Tensile and compressive stress components are observed reflecting the difference of the lattice parameter.

for fixed atomic positions

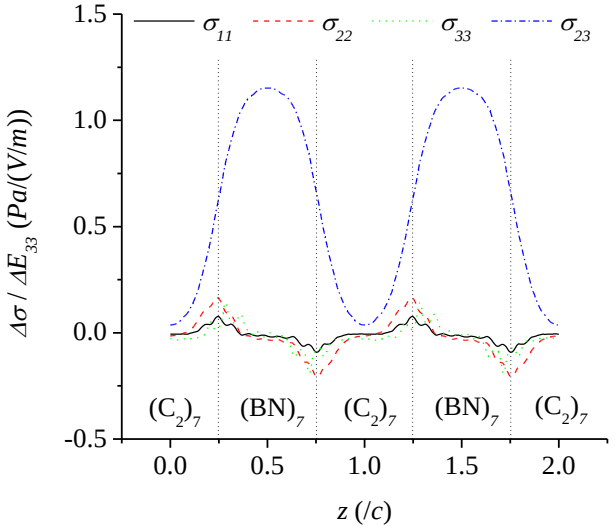

for relaxed atomic positions

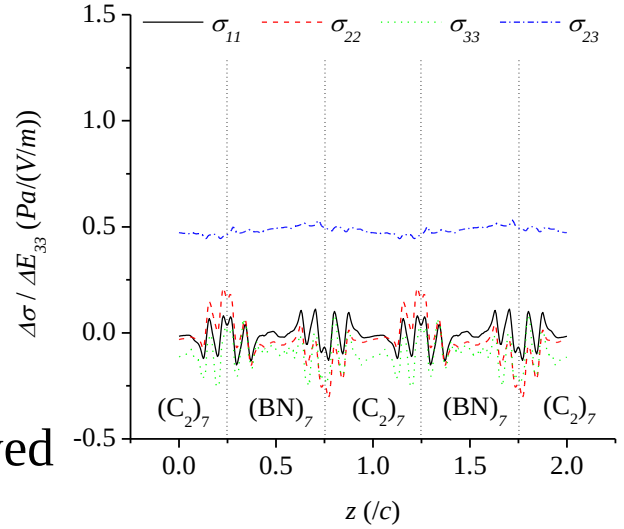

under static electric field

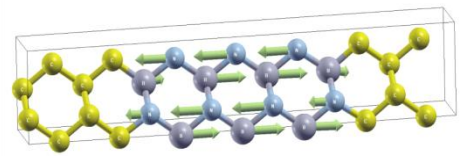

Applying electric field, shear stress appears in the BN layers reflecting forces acting on B or N atoms. Once atomic positions are relaxed, the shear stress is distributed over whole the region rather uniformly and its magnitude depends on the number of BN layers in the unit cell.

S. Ishibashi, T. Tamura, S. Tanaka, M. Kohyama and K. Terakura, Phys. Rev. B 76, 153310 (2007).

Linear and nonlinear polarizability profiles in LAO/STO superlattice

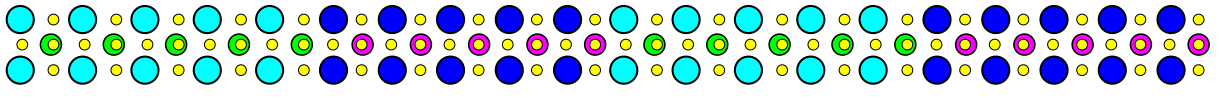

LAO STO

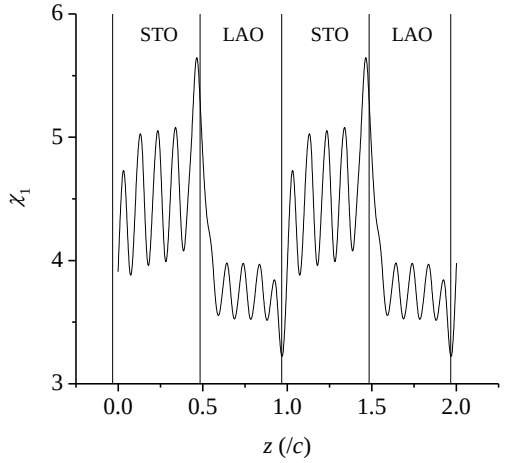

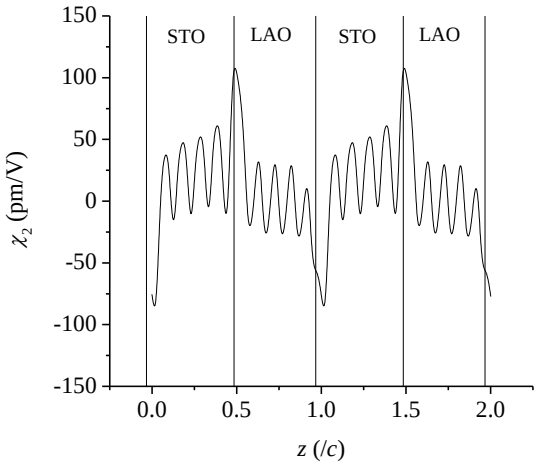

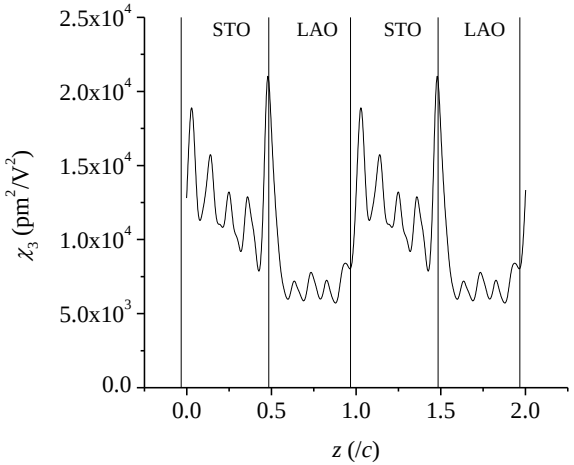

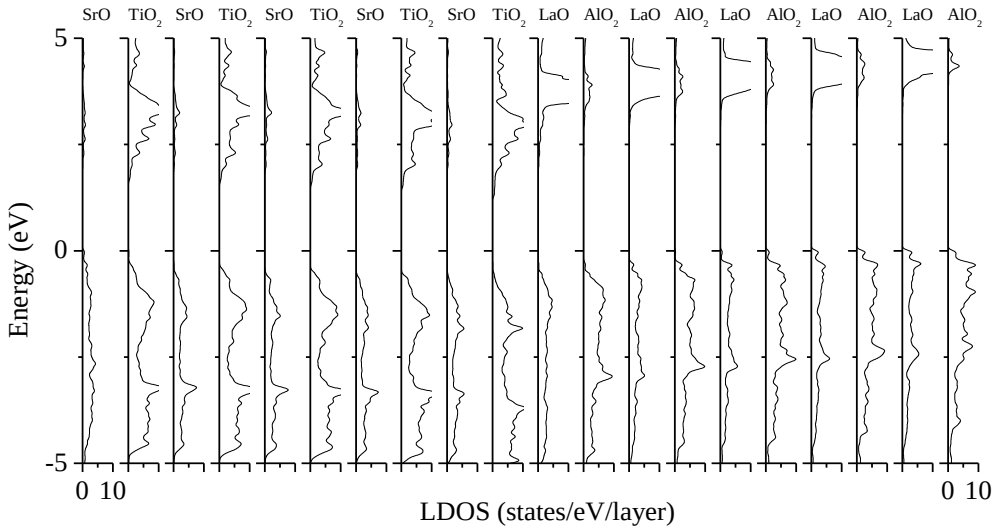

Polarizabilities up to the 3rd order are obtained by polynomial fitting:

$$\tilde{\tilde{p}}(z) = \tilde{\tilde{p}}_0(z) + \varepsilon_0\left(\chi_1(z)\tilde{\tilde{e}}(z) + \chi_2(z)\tilde{\tilde{e}}(z)^2 + \chi_3(z)\tilde{\tilde{e}}(z)^3\right)$$

where p and e represents polarization and local electric field, respectively.

S. Ishibashi and K. Terakura,
J. Phys. Soc. Jpn. **79**, 094701 (2010).

Crystal structure of antiferroelectric (AFE) SQA

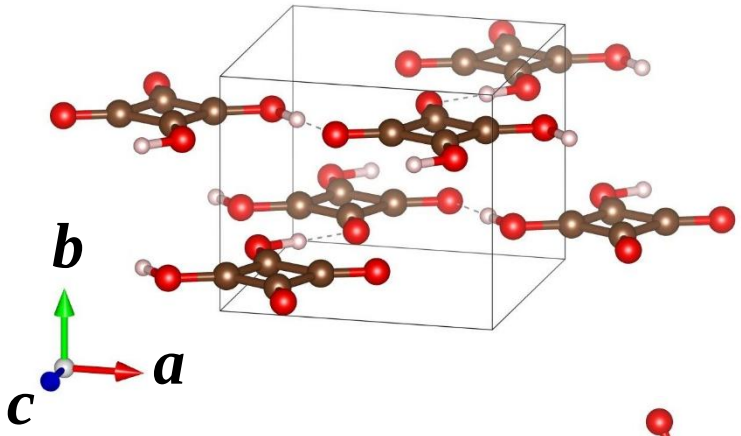

@25 ℃
a = 6.143 Å, b = 5.286 Å, c = 6.146 Å, β = 89.96°

Pace group $P2_1/m$

Calculated polarization for a sheet 11.6 μC cm^{-2}

$C_4H_2O_4$

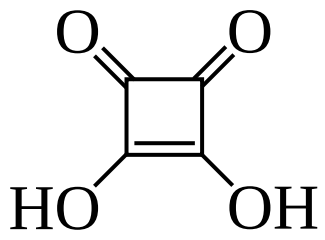

y = 0.25

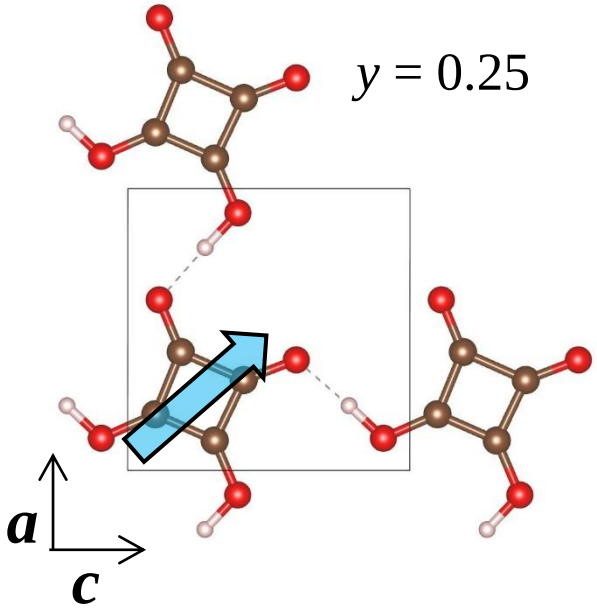

y = 0.75

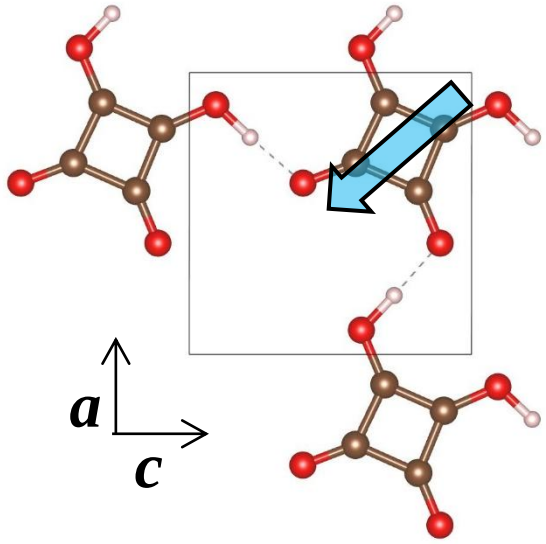

Electric-field-induced antiferroelectric-to-ferroelectric transition in SQA

S. Horiuchi, R. Kumai, and S. Ishibashi, Chem. Sci. **9**, 425 (2018).

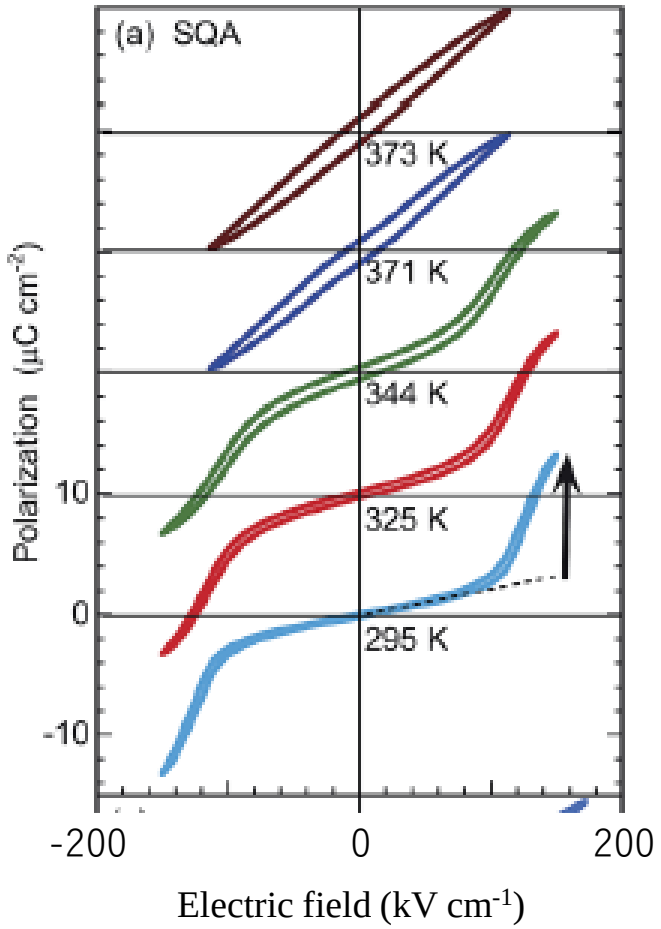

$\boldsymbol{E}$ // $[100]_{tetra}$

Possible ferroelectric (FE) phases

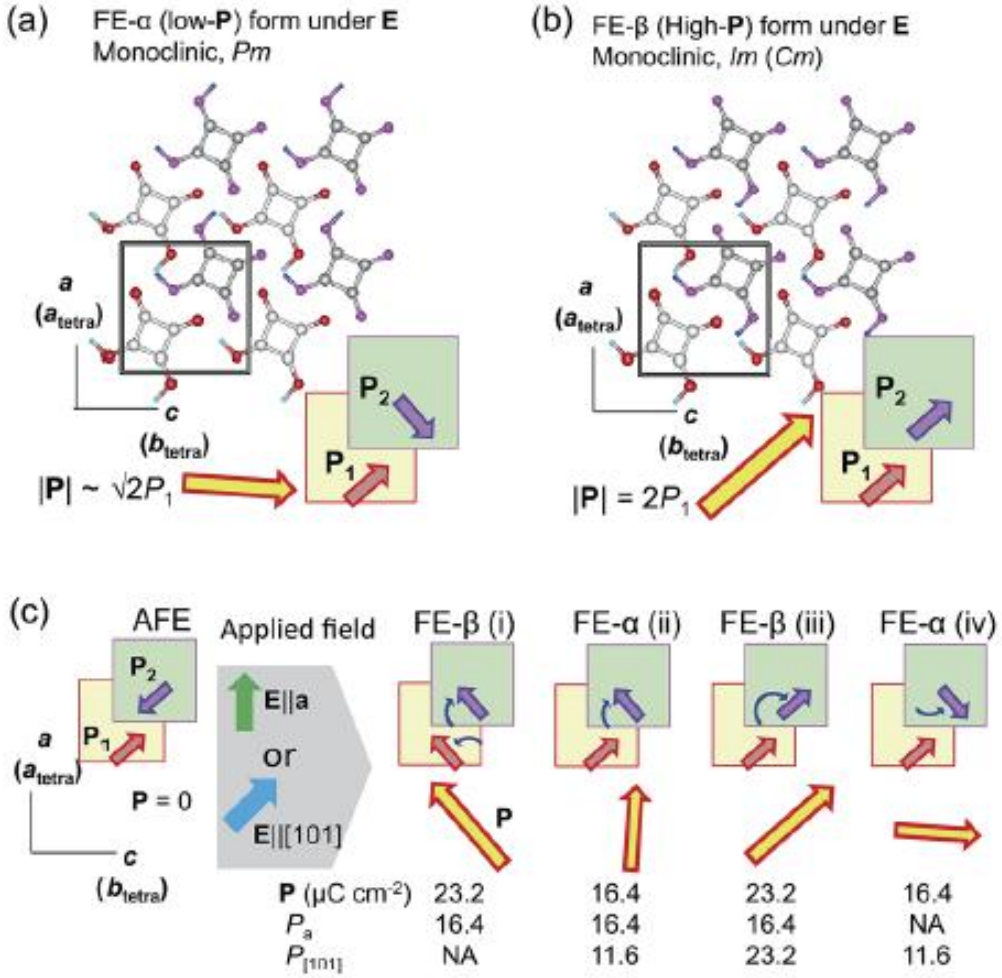

Calculated lattice parameters and hydrogen-bond lengths of SQA with various exchange-correlation functionals

S. Ishibashi, S. Horiuchi, and R. Kumai, Phys. Rev. B **97**, 184102 (2018).

In order to simulate the AFE-to-FE transition in SQA, the crystal structure of the AFE phase should be well reproduced.

	a (Å)	b (Å)	c (Å)	β (°)	$d_{O\cdots O}$ (Å)	
Expt. (15 K)	6.118	5.140	6.130	89.74	2.544	2.552
LDA	6.019 (−1.6)	4.919 (−4.3)	6.019 (−1.8)	90.00	2.413	2.413
GGA	6.192 (+1.2)	6.126 (+19.2)	6.203 (+1.2)	89.89	2.505	2.511
vdW-DF-cx	6.096 (−0.36)	5.381 (+4.7)	6.103 (−0.44)	89.97	2.484	2.486
rVV10	6.127 (+0.15)	5.143 (+0.06)	6.142 (+0.20)	89.92	2.537	2.542

Exp.: D. Semmingsen, Z. Tun, R. J. Nelmes, R. K. McMullan, and T. F. Koetzle, Z. Kristallogr. **210**, 934 (1995).
LDA: D. M. Ceperley and B. J. Alder, Phys. Rev. Lett. **45**, 566 (1980); J. P. Perdew and A. Zunger, Phys. Rev. B **23**, 5048 (1981).
GGA: J. P. Perdew, K. Burke, and M. Ernzerhof, Phys. Rev. Lett. **77**, 3865 (1996).
vdW-DF-cx: K. Berland and P. Hyldgaard, Phys. Rev. B **89**, 035412 (2014).
rvv10: O. A. Vydrov and T. Van Voorhis, J. Chem. Phys. **133**, 244103 (2010); R. Sabatini, T. Gorni, and S. de Gironcoli, Phys. Rev. B **87**, 041108(R) (2013).

The rvv10 functional gives the best results.

Simulation of field-induced phase transition in SQA (*x*//*a*, *z*//*c**)

S. Ishibashi, S. Horiuchi, and R. Kumai, Phys. Rev. B **97**, 184102 (2018).

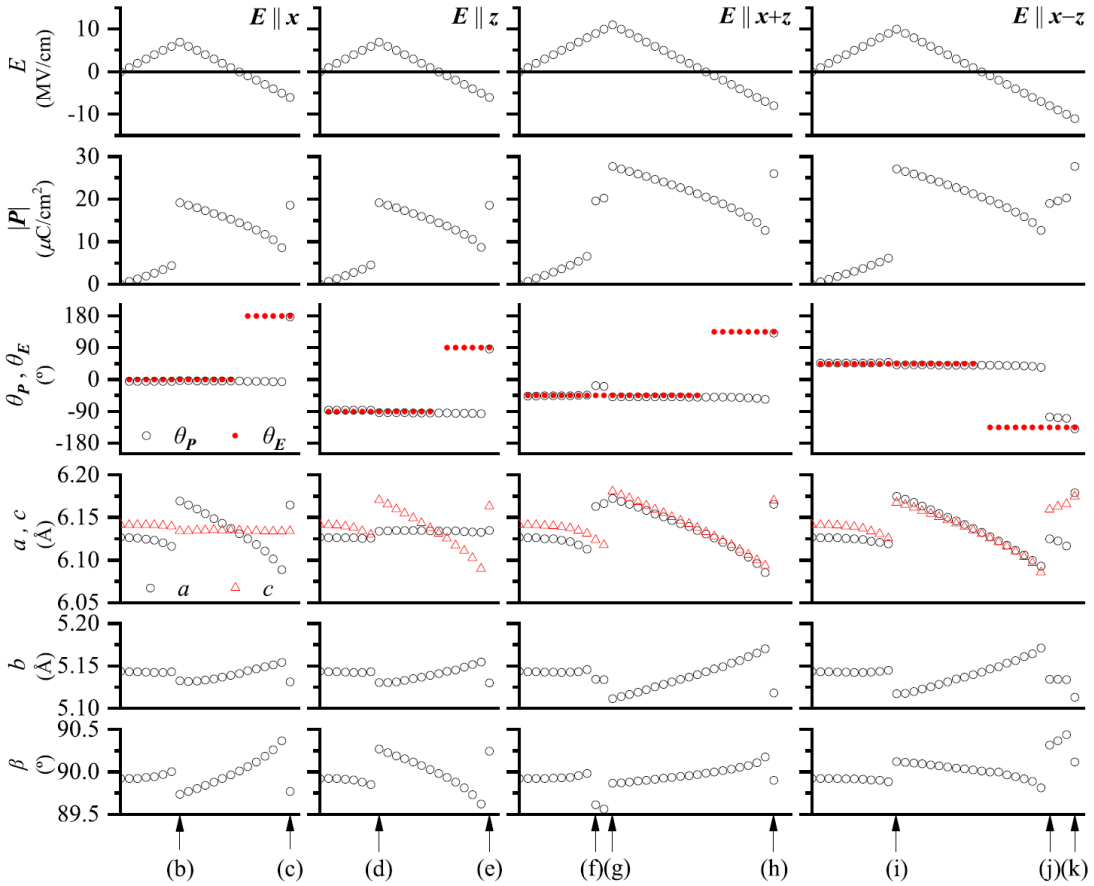

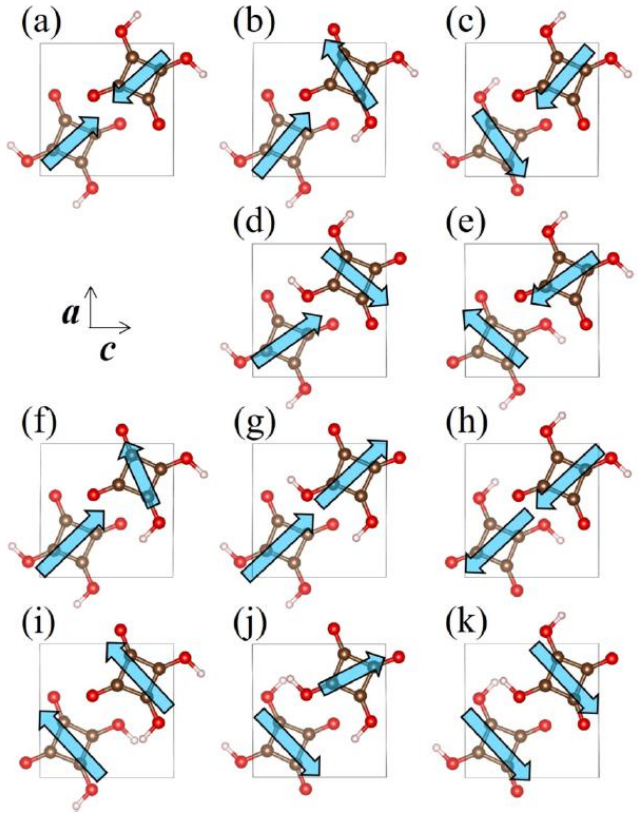

Polarization@E=0:
FE-α 14.5 μC cm^{-2}
FE-β 20.6 μC cm^{-2}

Piezoelectric constant d_{11} or d_{33}: ~ 10. pm/V

Discrepancies between experiment and calculation

- The switching field is nearly two orders higher in the calculation.
- After the electric field is removed, for the calculation, the system remains in the FE phase, while, for the experiment, the system returns to the AFE phase.

There is a finite barrier between the AFE and the FE-α or FE-β phase.

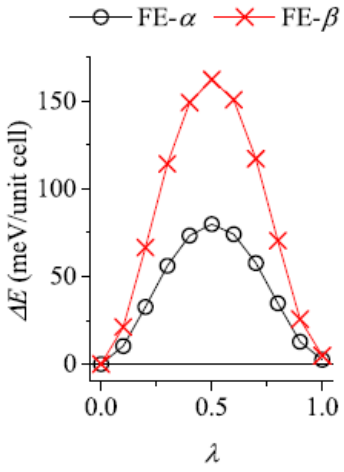

Possible reasons

- Equivalent H atoms in the repeated unit cells move at the same time in the calculation, while domain walls move in reality.
- There is no surface and no defect in the calculation.
- The finite temperature effect is not considered in the present calculations

Cf.

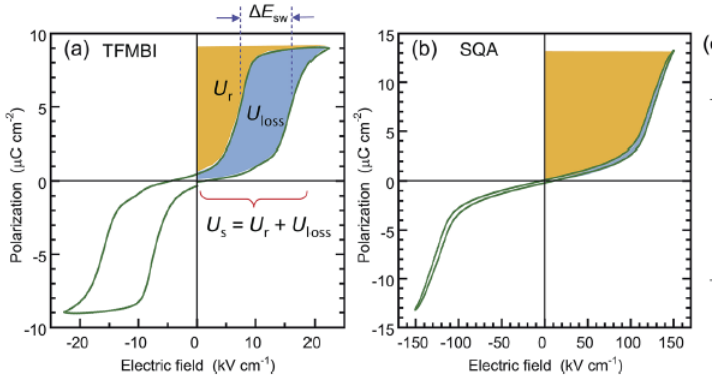

SQA is expected as a promising candidate for an energy storage material.

S. Horiuchi, R. Kumai, and S. Ishibashi, Chem. Sci. **9**, 425 (2018).

Reproducibility of structural parameters by vdW-DFT

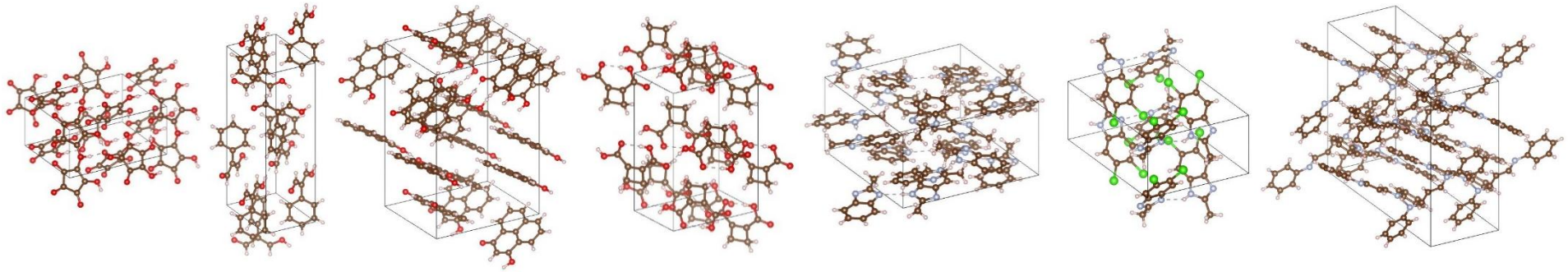

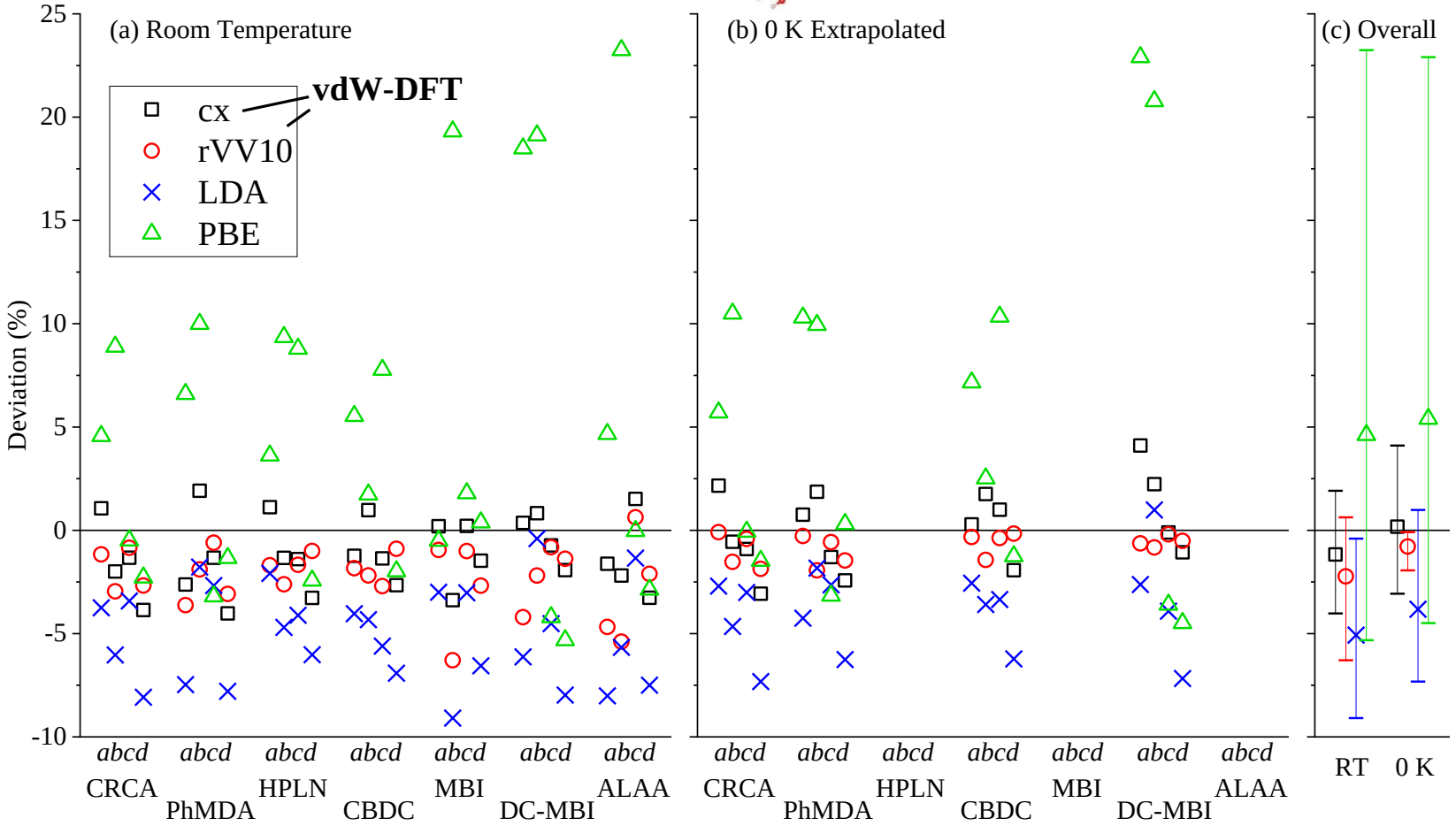

a, *b*, *c*:
lattice parameters
d:
average hydrogen
bond length

S. Ishibashi, S. Horiuchi, and R. Kumai, Phys. Rev. Mater. **5**, 094409 (2021).

Simulation of direct and converse piezoelectric effects

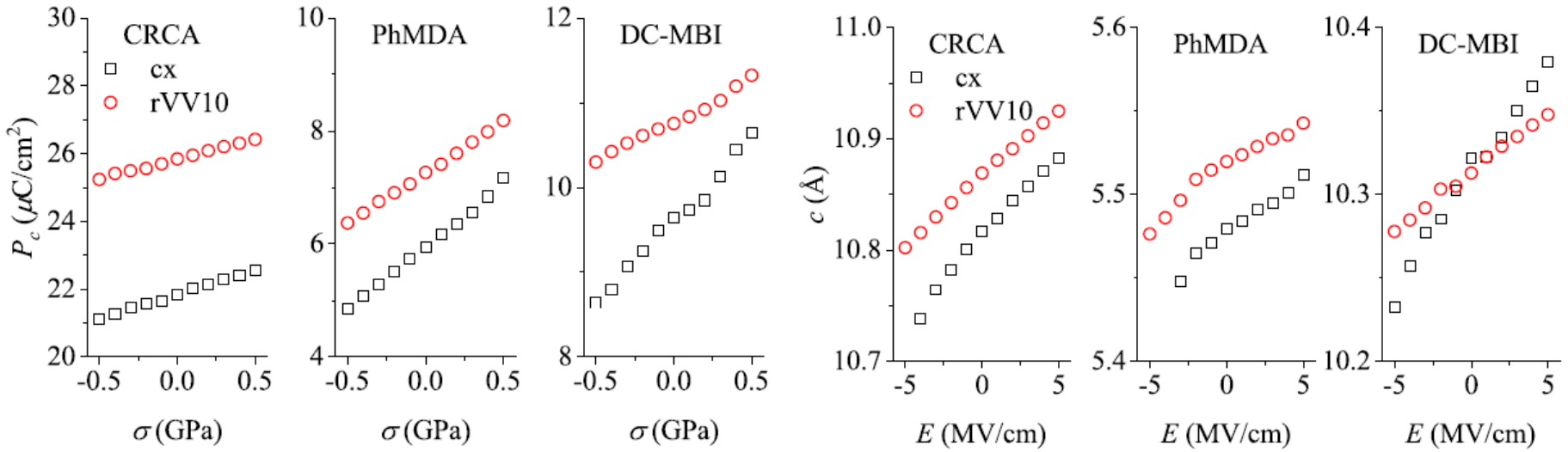

	Direct (pC/N)			Converse (pm/V)			E_3^Y (GPa)	
	cx	rVV10	EXP	cx	rVV10	EXP	cx	rVV10
CRCA	13.8	10.8	15.1	13.6	10.9	7.6	102.3	103.3
PhMDA	17.2	12.5	10.4	11.5	8.3	4.3	13.1	14.4
DC-MBI	15.3	7.8	12.2	13.2	6.8		24.2	38.7

The difference between the two van der Waals functionals (cx and rVV10) is larger for the N–H…N case than for the O–H…O case.

S. Ishibashi, S. Horiuchi, and R. Kumai, Phys. Rev. Mater. **5**, 094409 (2021).

Crystal structure of DHBA (left) and Hdabco-ReO_4 (right)

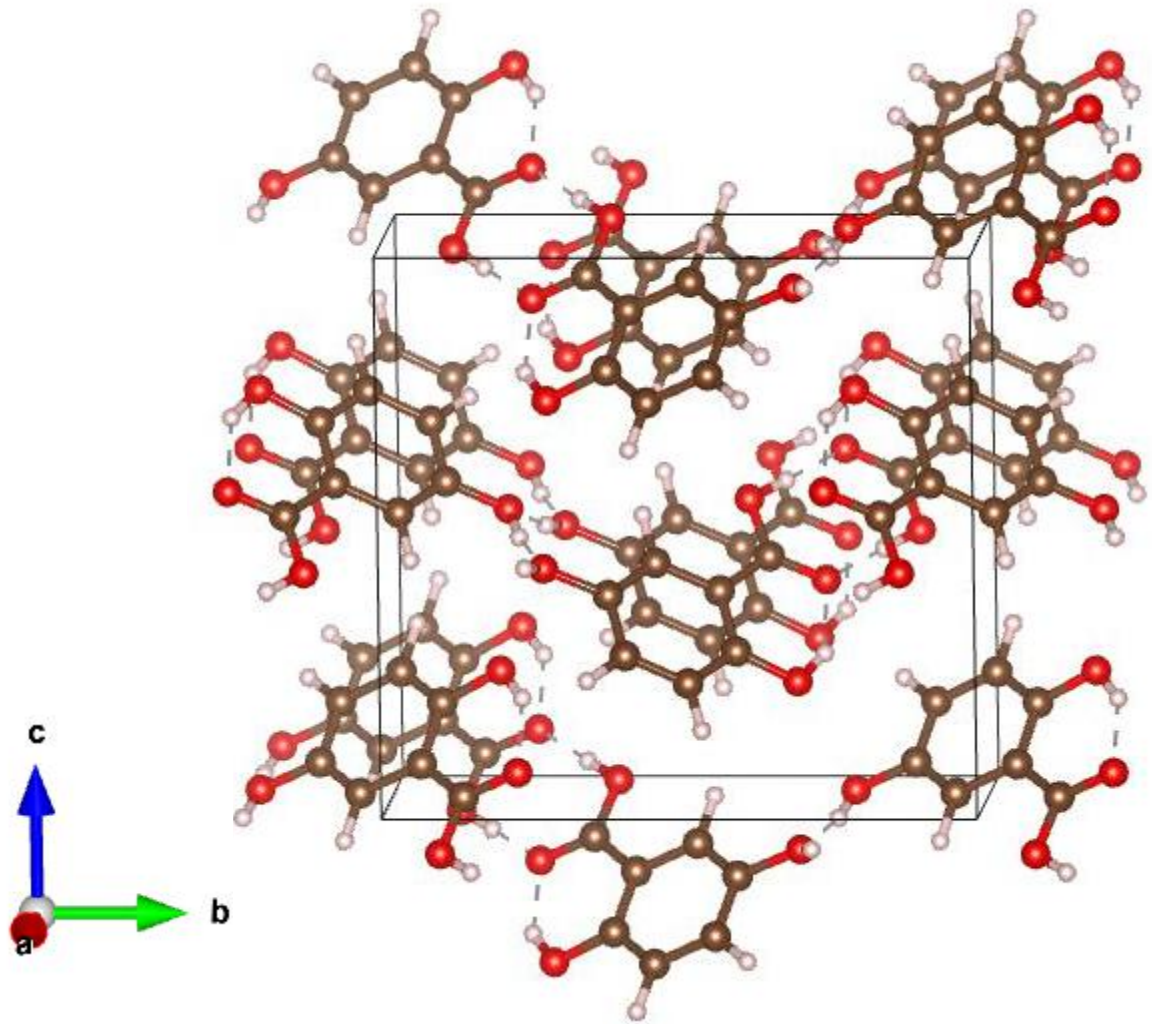

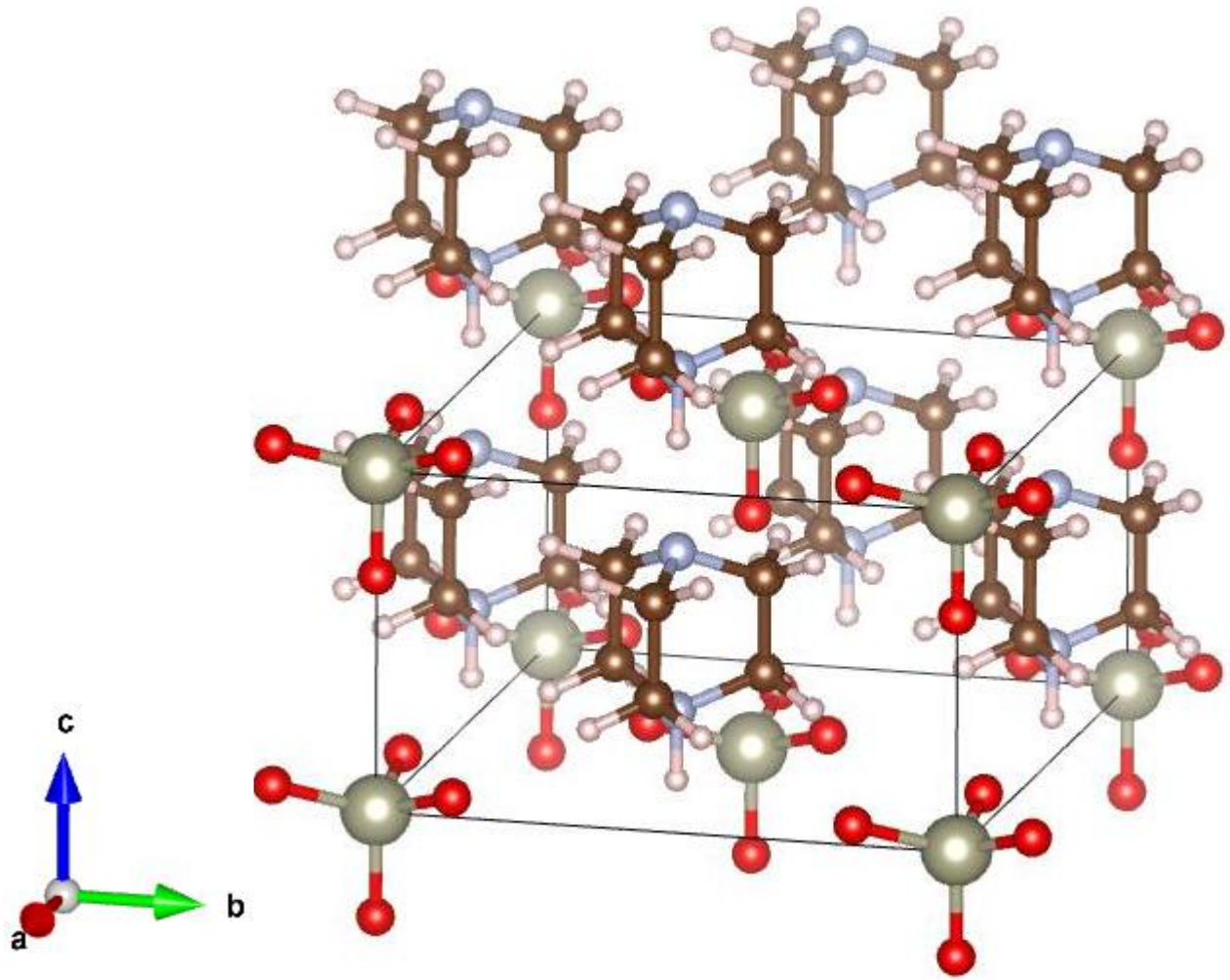

Two possible ferroelectric switching schemes

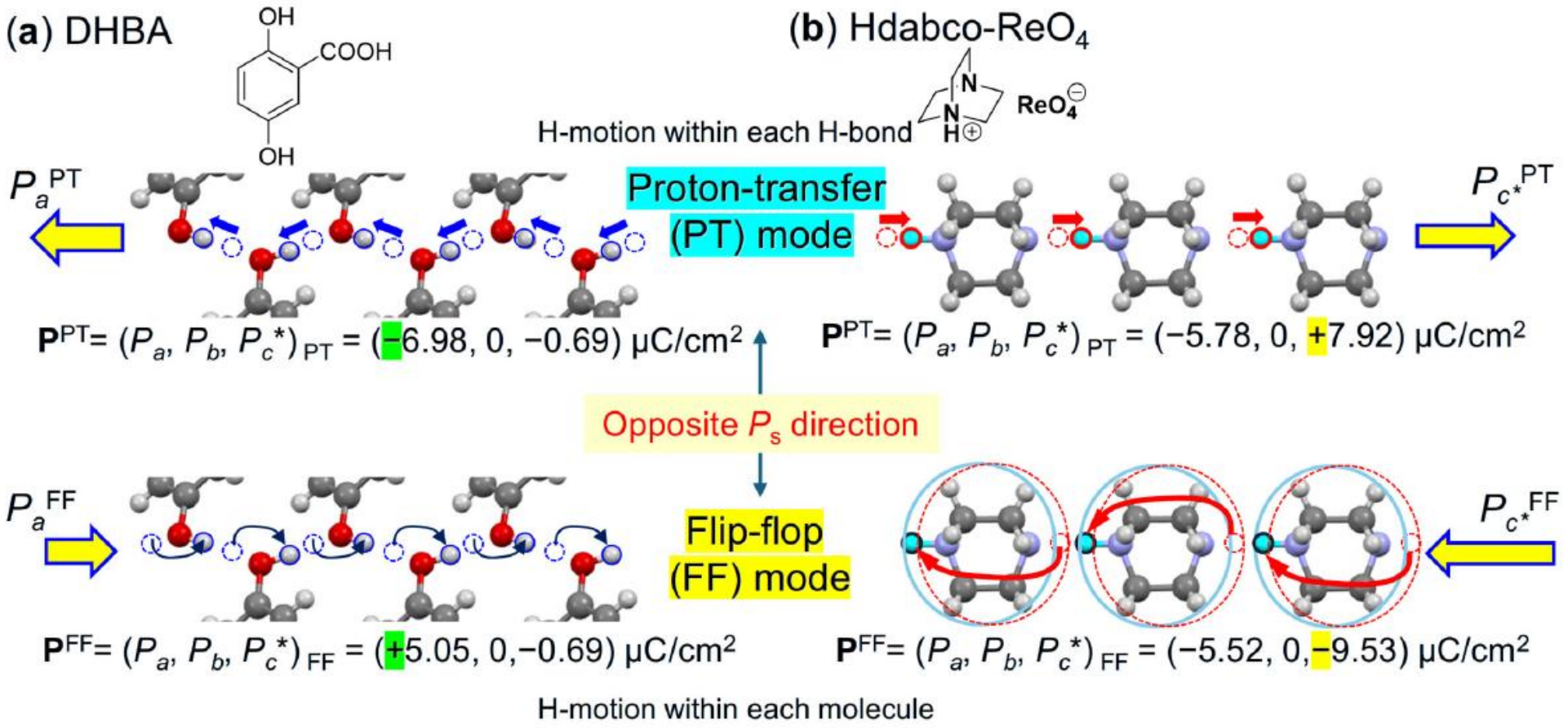

S. Horiuchi, H. Minemawari, J. Tsutsumi, and S. Ishibashi, Crystals **15**, 736 (2025).

Berry phase variation during ferroelectric switching: DHBA

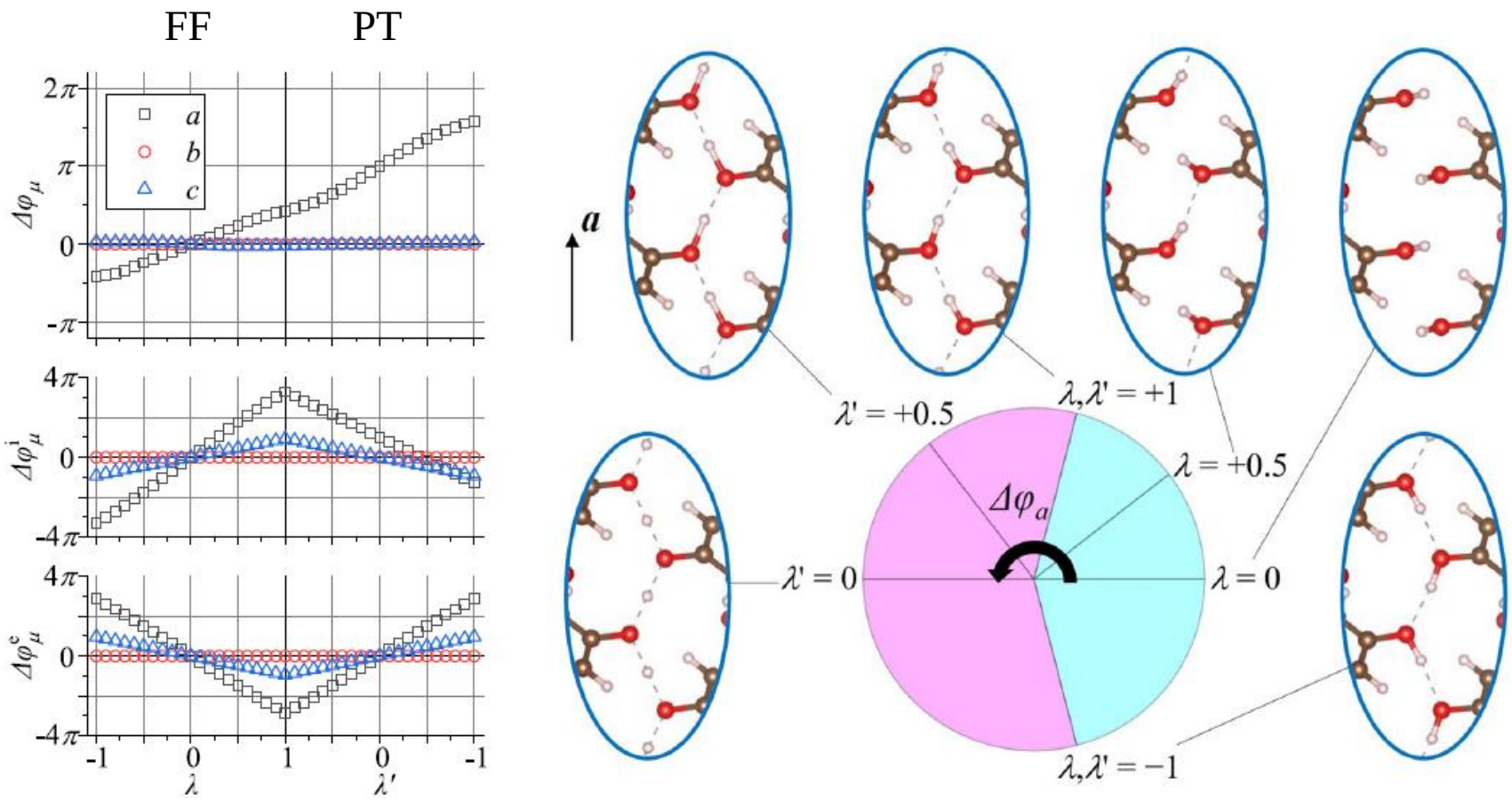

Figure 1. Berry phase variation $\Delta\varphi_\mu$ ($\mu = a, b, c$) as a function of λ or λ' for DHBA. Since there are relationships of $\Delta\varphi_a(\lambda' = -1) - \Delta\varphi_a(\lambda = -1) = 2\pi$ and $\Delta\varphi_a(\lambda' = 0) - \Delta\varphi_a(\lambda = 0) = \pi$, $\Delta\varphi_a$ is plotted with a circular chart to visualize the interrelationship between the λ and λ' processes. Insets are snapshots of the hydrogen-bonded network.

Polarization vector ($\mu C/cm^2$)
FF: (5.05, 0, −0.69)
PT: (−6.98, 0, −0.69)

From $\lambda = -1$ to $\lambda' = -1$, the fractional coordinates of the four switching hydrogen atoms move
(0.480,−0.027, 0.016),
(0.520, 0.027,−0.016),
(0.480, 0.027, 0.016), and
(0.520,−0.027,−0.016),
respectively.
Their sum (2, 0, 0) is consistent with the polarization change of $2|e|R_a/\Omega$, which corresponds to the 2π change of the ionic part of the Berry phase.

GGA-PBE, with the H positions optimized

S. Ishibashi, R. Kumai, and S. Horiuchi, Sci. Rep. **13**, 8810 (2023).

Berry phase variation during ferroelectric switching : Hdaboco-ReO_4

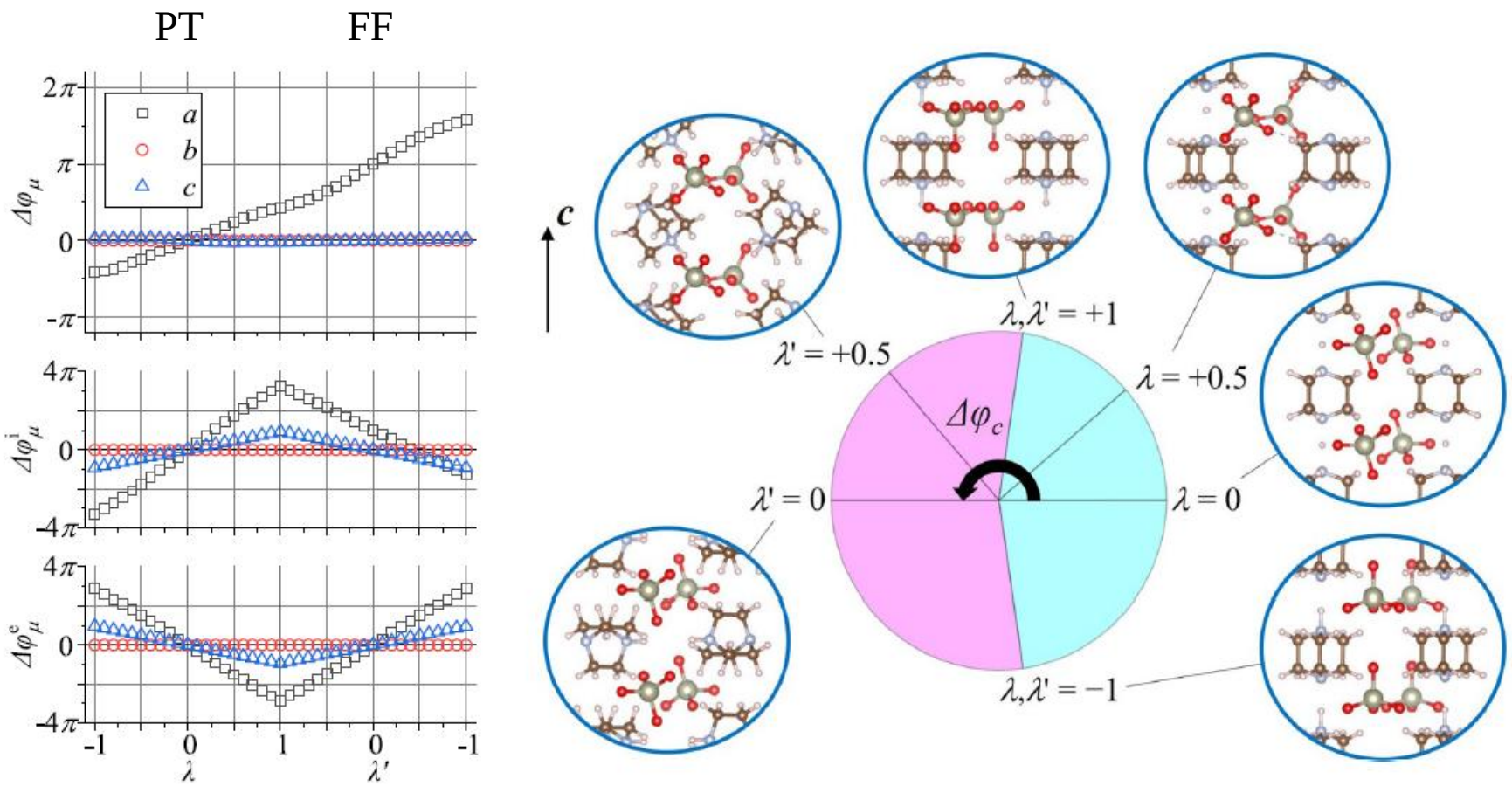

Figure 2. Berry phase variation $\Delta\varphi_\mu$ ($\mu = a, b, c$) as a function of λ or λ' for Hdabco-ReO_4. Similar to Fig. 1, $\Delta\varphi_c$ is plotted with a circular chart. Insets represent structural snapshots at several λ or λ' values.

Polarization vector ($\mu C/cm^2$)
PT: (−5.78, 0, 7.92)
FF: (−5.52, 0, −9.53)

From $\lambda = -1$ to $\lambda' = -1$, the two switching hydrogen atoms in the unit cell travel the unit-cell length along *c*.
This is consistent with the 2π change of the ionic part of the Berry phase.

GGA-PBE, with the H positions optimized

S. Ishibashi, R. Kumai, and S. Horiuchi, Sci. Rep. **13**, 8810 (2023).

Why the sign of the piezoelectric coefficient can be used to decide which mode occurs?

Direct piezoelectric effect:

- If stress is applied along a direction where finite polarization is observed, the polarization changes from $\boldsymbol{P}$ to $\boldsymbol{P}+\Delta\boldsymbol{P}$ (generally, $|\boldsymbol{P}|\gg|\Delta\boldsymbol{P}|$).
- Since the piezoelectric effect is due to a small deformation and is not accompanied by the ferroelectric switching, the change in polarization as a vector $\Delta\boldsymbol{P}$ is uniquely defined and independent of the ferroelectric switching mechanism.
- If we assume $\boldsymbol{P}=(P_x,0,0)$ and ΔP_x is positive, $|P_x|<|P_x+\Delta P_x|$ when P_x is positive, whereas $|P_x|>|P_x+\Delta P_x|$ when P_x is negative.
- The direct piezoelectric coefficient can be evaluated from the change in the polarization amplitude upon applying stress.
- Thus, the sign of the direct piezoelectric coefficient depends on the sign of P_x.
- For both DHBA and Hdabco-ReO_4, because the signs of the polarization components along the hydrogen-bond directions differ according to the switching mechanism, the sign of the direct piezoelectric coefficient can elucidate the actual switching process.

Why the sign of the piezoelectric coefficient can be used to decide which mode occurs?

Converse piezoelectric effect:

- The converse piezoelectric effect corresponds to the strain as a first-order response against an induced electric field $\boldsymbol{E}$.
- We assume that the polarization and electric-field vectors have finite amplitudes only for their x-components P_x and E_x.
- By applying E_x, a finite strain $\boldsymbol{\varepsilon}$ is induced. Here ε_{xx} is assumed to be positive.
- Generally, the converse piezoelectric coefficient is evaluated by adjusting the E_x sign to be the same as that of P_x.
- If the sign of P_x differs, the sign of the evaluated converse piezoelectric coefficient should differ.
- Hence, the switching modes can be distinguished.

Lattice Parameters obtained by vdW-DFT

(EXP0: the 0-K extrapolated values from the X-ray diffraction results)

	DHBA			Hdabco-ReO_4		
	EXP0	cx	rVV10	EXP0	cx	rVV10
a (Å)	4.8719	4.7990 (−1.5)	4.8414 (−0.6)	10.049	10.279 (+2.3)	10.008 (−0.4)
b (Å)	11.801	11.974 (+1.5)	11.859 (+0.5)	8.685	9.036 (+4.0)	8.827 (+1.6)
c (Å)	10.910	11.339 (+3.9)	10.809 (−0.9)	5.3108	5.3013 (−0.2)	5.3325 (+0.4)
β (°)	91.514	91.966	91.702	89.94	89.801	90.051

by PBE/PBEsol

	DHBA			Hdabco-ReO_4		
	EXP0	PBE	PBEsol	EXP0	PBE	PBEsol
a (Å)	4.8719	4.9132 (+0.8)	4.7060 (−3.4)	10.049	10.542 (+4.9)	10.425 (+3.7)
b (Å)	11.801	12.021 (+1.9)	11.889 (+0.7)	8.685	9.479 (+9.1)	9.032 (+4.0)
c (Å)	10.910	12.842 (+17.7)	12.160 (+11.5)	5.3108	5.3859 (+1.4)	5.2479 (−1.2)
β (°)	91.514	86.547	89.144	89.94	90.147	88.982

Simulated direct/converse piezoelectric effects

DHBA (based on the polarization for FF)

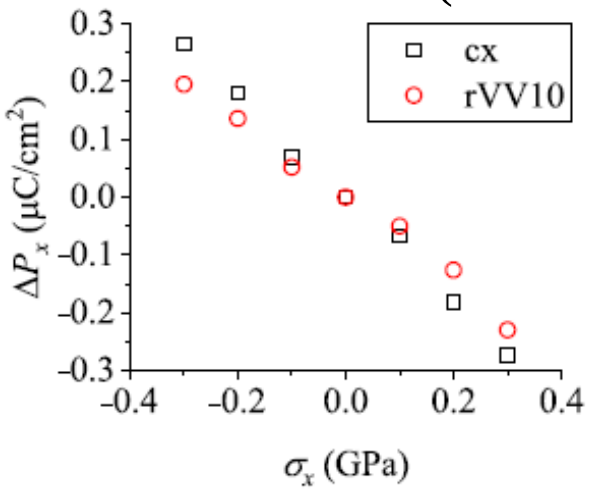

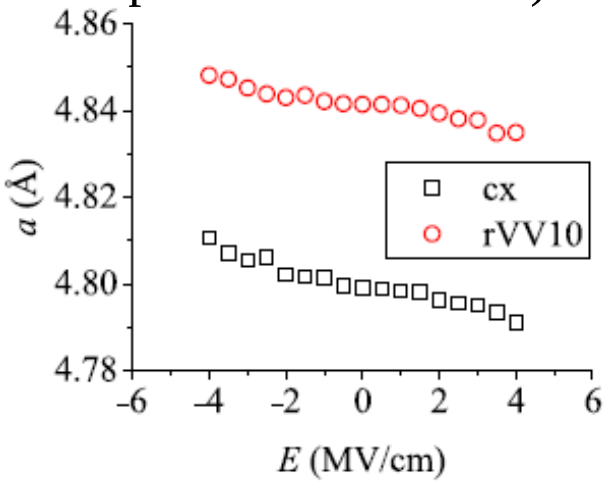

Hdabco-ReO_4 (based on the polarization for PT)

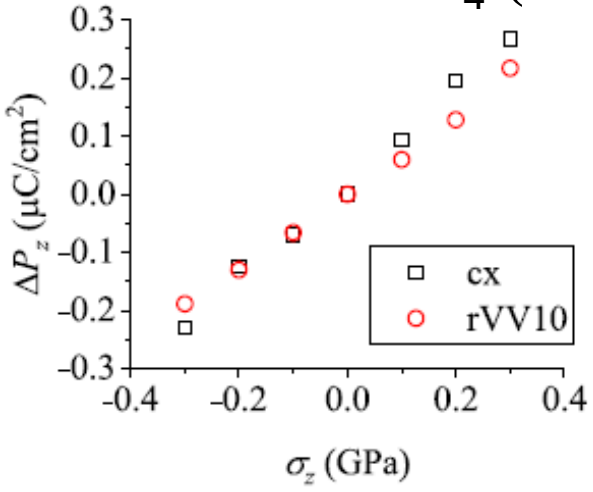

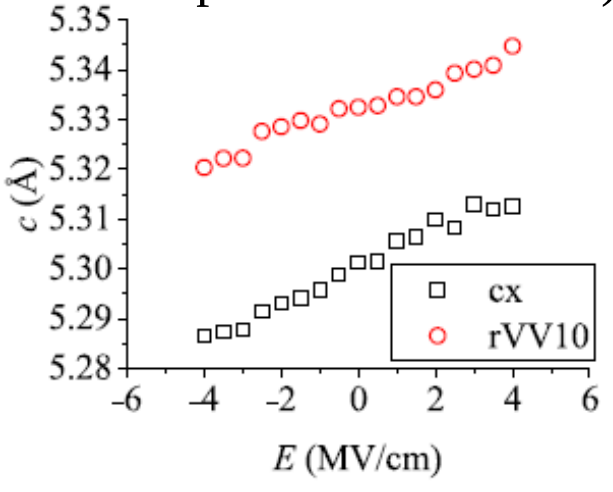

$$d_{11} = \frac{1}{2\pi}\frac{2|e|}{\Omega}\sum_{\alpha}\frac{\mathrm{d}\varphi_\alpha}{\mathrm{d}\sigma_1}R_{\alpha 1}$$

cx
−8.86 pC/N, −4.17 pm/V
rVV10
−6.79 pC/N, −2.95 pm/V
exp.
−7.7 pC/N, −4.8 pm/V

Table 2 Polarization vectors (μC/cm^2) of DHBA evaluated by cx or rVV10 assuming a FF or PT process.

	FF	PT
cx	(5.62, 0., −0.48)	(−6.42, 0., −0.48)
rVV10	(5.77, 0., −0.49)	(−6.26, 0., −0.49)

Table 3 Polarization vectors (μC/cm^2) of Hdabco-ReO_4 evaluated by cx or rVV10 assuming the PT or FF modes.

	PT	FF
cx	(−5.72, 0., 7.23)	(−5.46, 0., −10.22)
rVV10	(−5.71, 0., 8.20)	(−5.45, 0., −9.25)

d_{33}

cx
+8.20 pC/N, +6.86 pm/V
rVV10
+6.64 pC/N, +5.03 pm/V
exp.
+5.1 pC/N, N/A

S. Ishibashi, R. Kumai, and S. Horiuchi, Sci. Rep. **13**, 8810 (2023).

Layer-resolved local stress

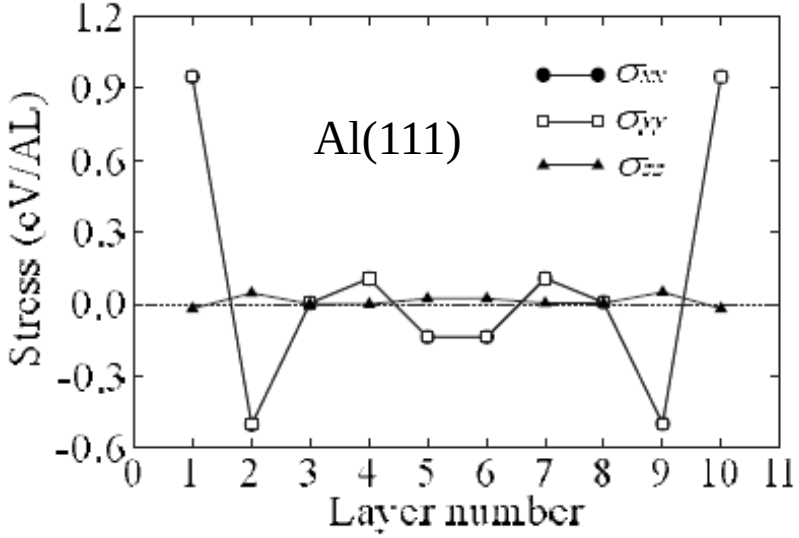

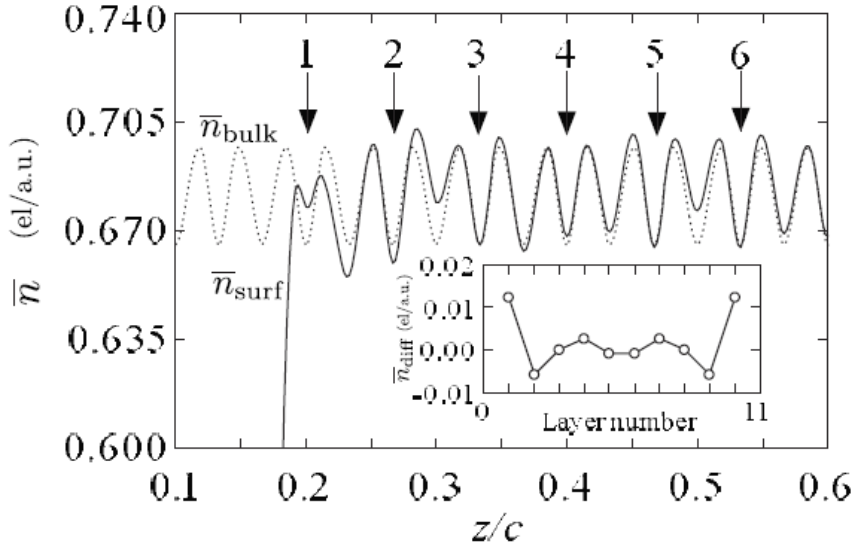

Positive stress values mean tensile stress.

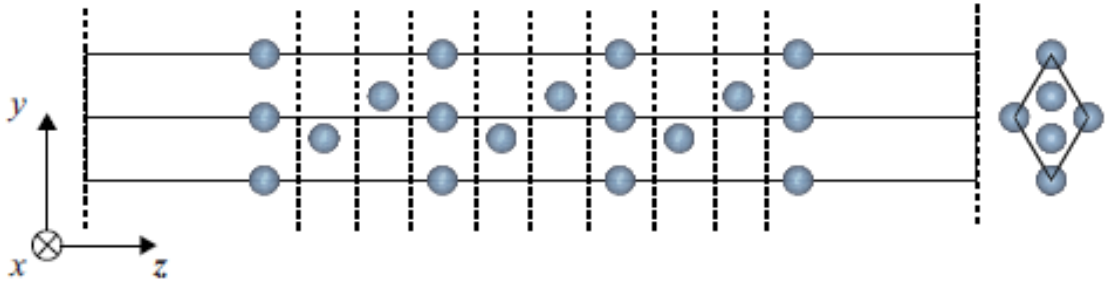

Y. Shiihara, M. Kohyama, and S. Ishibashi, Phys. Rev. B 81, 075441 (2010).

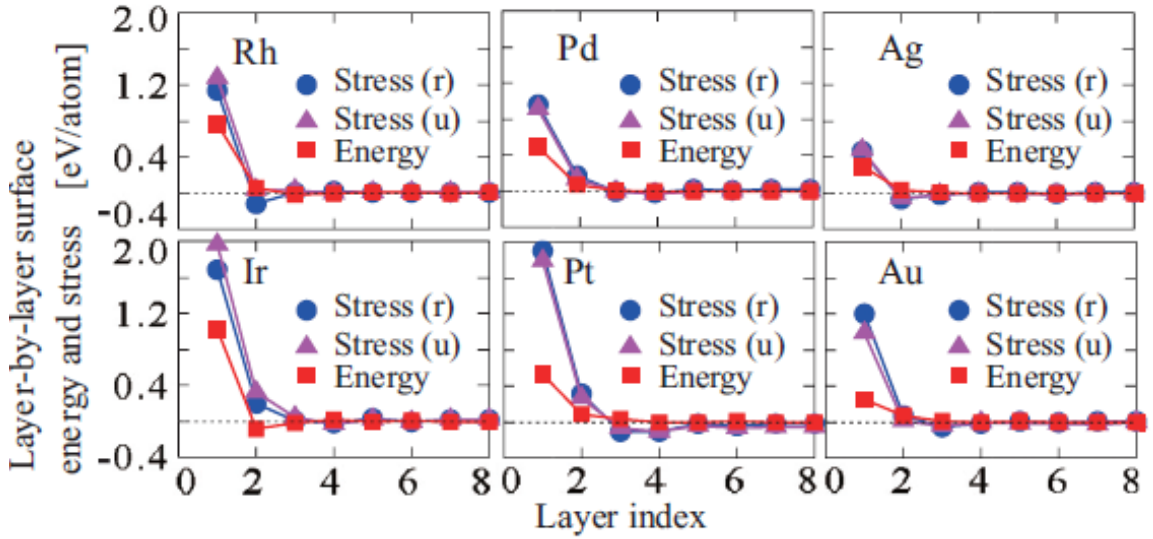

Y. Shiihara, M. Kohyama, and S. Ishibashi, Phys. Rev. B 87, 125430 (2013).

15 kinds of BCC equiatomic disordered alloys including refractory high-entropy alloys modeled by the Special Quasirandom Structure (SQS) method*

*A. Zunger *et al.*, Phys.Rev. Lett. 65, 353 (1990).

Binary (4 × 4 × 4 conventional cell, 128 atoms)
VW, MoTa

Ternary (3 × 3 × 3 conventional cell, 54 atoms)
VNbW, VTaW, ZrNbHf, NbMoTa

Quaternary (4 × 4 × 4 conventional cell, 128 atoms)
TiVNbTa, VNbMoTa, VNbTaW, NbMoTaW

Quinary (5 × 5 × 5 primitive cell, 125 atoms)
TiVNbMoTa, TiVNbTaW, TiZrNbHfTa, TiZrMoHfTa, VNbMoTaW

Evaluation of local atomic parameters using the Bader domain decomposition*

*M. Yu and D. R. Trinkle, J. Chem. Phys. **134**, 064111 (2011).

Volume: Bader volume ≡ Volume of Bader domain
Charge: Bader charge ≡ Charge within Bader domain
Stress: Integral of **stress density** over Bader domain

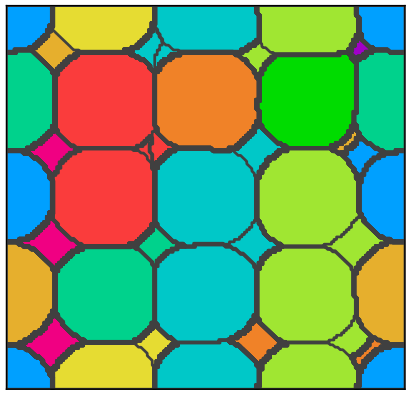

$$\nabla\rho \cdot \hat{n} = 0$$

Strong correlation between the three parameters

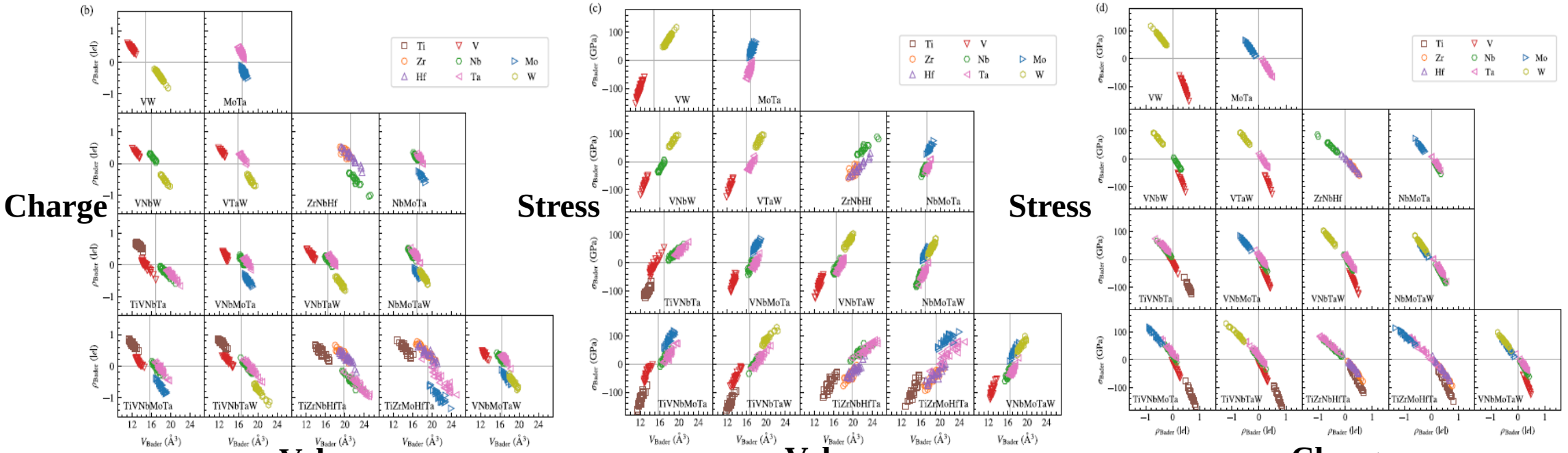

S. Ishibashi, Y. Ikeda, F. Körmann, B. Grabowski, and J. Neugebauer, Phys. Rev. Mater., **4**, 023608 (2020).

Behavior of atomic parameters in equiatomic disordered alloys

・Even for the same elements in the same alloy, the distribution of atomic parameters is unexpectedly wide, indicating the existence of large effects of local composition.

・For each alloy and element, a significant linear correlation is observed between the atomic parameters.

・ The average atomic parameters of each element in an alloy can be related to the valence electron concentration (VEC) of the alloy (a clear linear correlation as shown in the figure on the right).

The atomic stress for each alloy and element can be approximated by a linear equation using the VECs of the 1st and 2nd nearest neighbor sites.

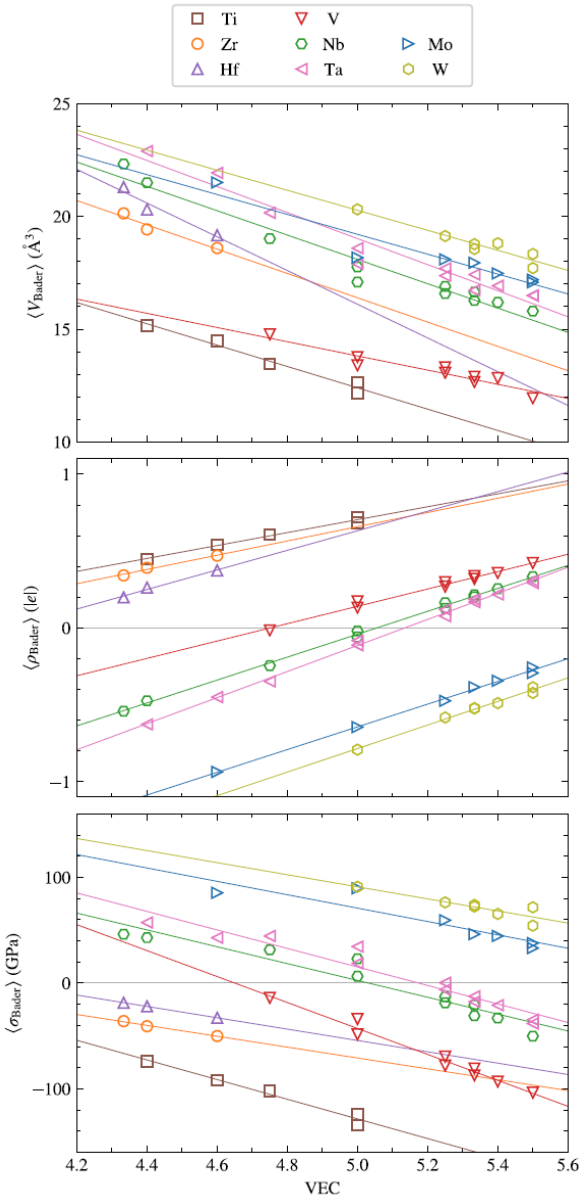

S. Ishibashi, Y. Ikeda, F. Körmann, B. Grabowski, and J. Neugebauer,
Phys. Rev. Mater., **4**, 023608 (2020).

Stress density combined with the effective screening medium (ESM) method*

*M. Otani and O. Sugino, Phys. Rev. B **73**, 115407 (2006).

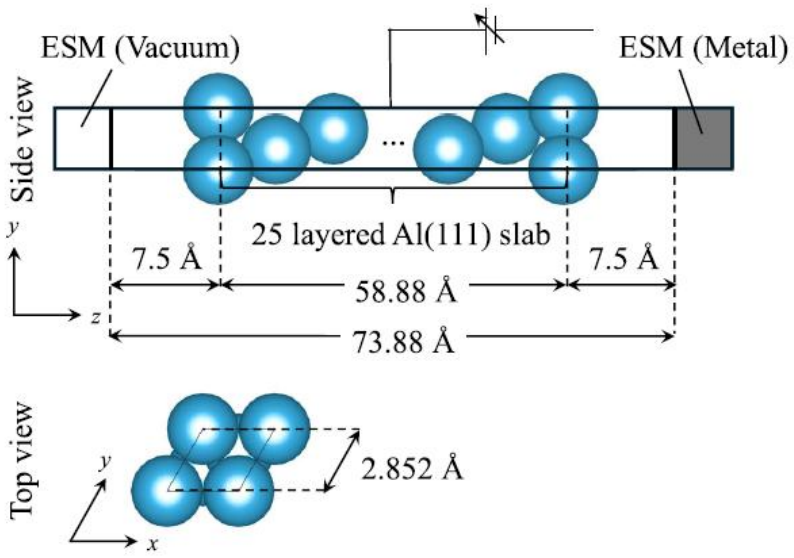

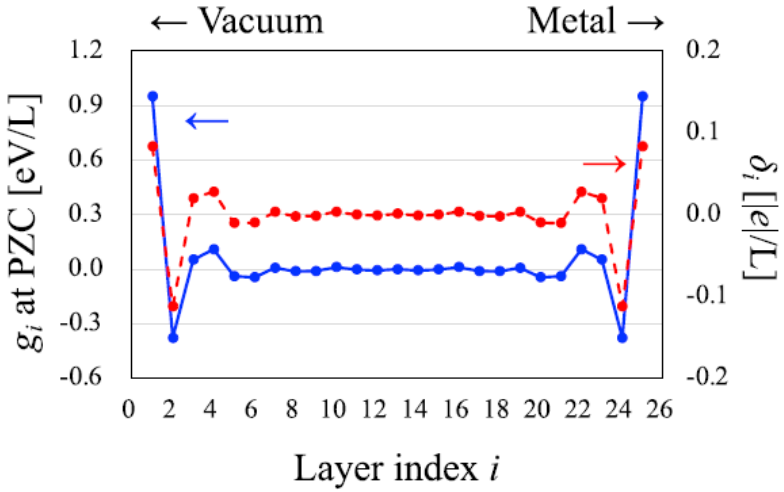

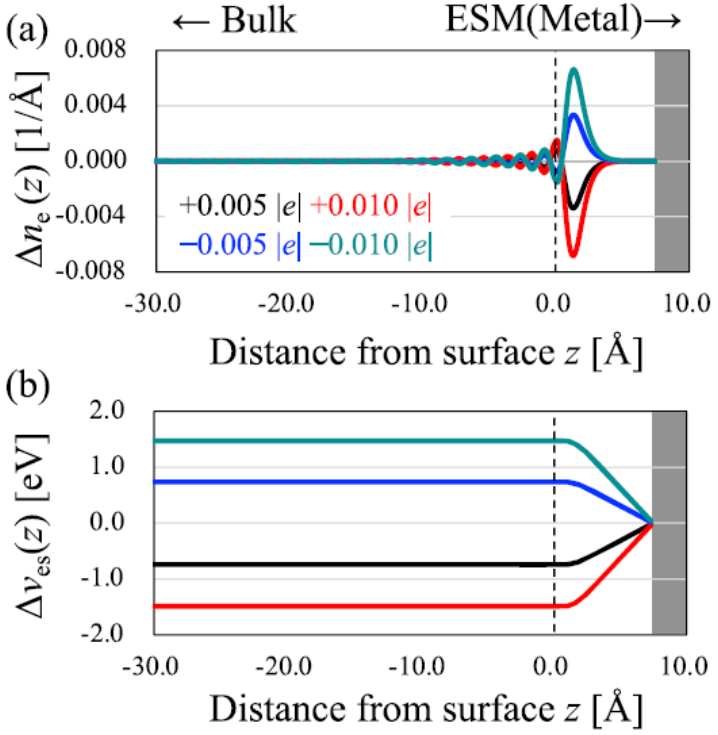

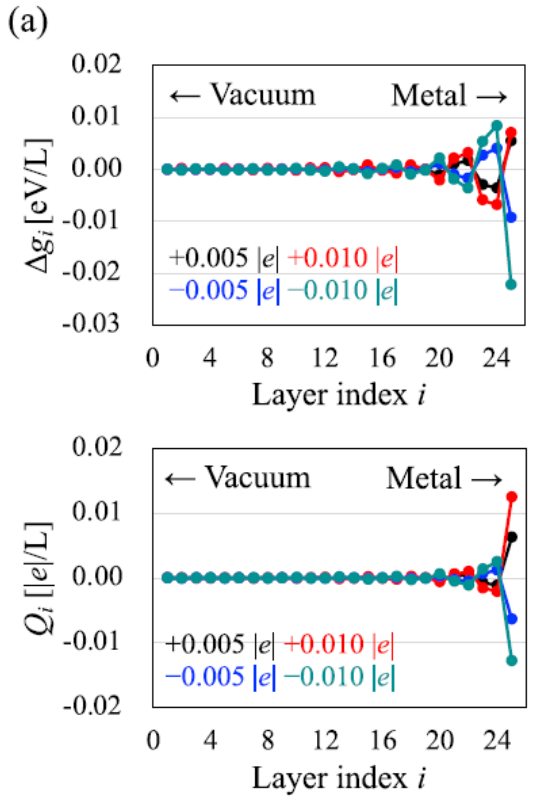

Layer-resolved local stress under a finite bias voltage can be obtained.

S. Hagiwara, S. Ishibashi, and M. Otani, Phys. Rev. B 110. 155409 (2024).

Outline

Overview of the computational code QMAS

Applications of QMAS's distinctive calculation functions

- Positron annihilation
- Static electric field
- Stress density

Release of QMAS Fortran90 beta version

QMAS initiatives at the Center for Computational Sciences, University of Tsukuba

by Dr. Satoshi HAGIWARA and Professor Minoru OTANI

Concerns about the older versions of QMAS

- Copyright issues regarding free software related to symmetry and numerical calculations
- Coded in FORTRAN 77
- Labyrinthine program structures due to repeated tuning
- Memory usage per core

Development of the new version of QMAS

- Rewriting the program from FORTRAN 77 to Fortran 90
- Replacing the TSPACE part with “Automatic symmetry finder”
- Improvements of the MPI parallelization
  = Triple parallelization for ***k*** points, bands, and mesh+FFT, Memory saving
- Speeding up diagonalization routines with ELPA
- Enhancements of surface and interface calculation functions using ESM

The beta version has been released at https://qmas.jp.